The Venus Global Ionosphere-Thermosphere Model (V-GITM): A Coupled Thermosphere and Ionosphere Formulation

[1]Brandon M. Ponder, [2]Aaron J. Ridley, [2]Stephen W. Bougher, [3]David Pawlowski, [4]Amanda Brecht

[1]Lockheed Martin Missiles and Fire Control, Grand Prairie, Texas, USA

[2]Department of Climate and Space Sciences and Engineering, University of Michigan, Ann Arbor, MI USA

[3]Physics and Astronomy Department, Eastern Michigan University, Ypsilanti, MI, USA

[4]NASA Ames Research Center, Moffett Field, CA, USA

Abstract

This paper introduces the new Venus Global Ionosphere Thermosphere Model (V-GITM) which incorporates the terrestrial GITM framework with Venus-specific parameters, ion-neutral chemistry, and radiative processes in order to simulate some of the observable features regarding the temperatures, composition, and dynamical structure of the Venus atmosphere from 70 km to 170 km. Atmospheric processes are included based upon formulations used in previous Venus GCMs, several augmentations exist, such as improved horizontal and vertical momentum equations and tracking exothermic chemistry. Explicitly solving the momentum equations allows for the exploration of its dynamical effects on the day-night structure. In addition, V-GITM's use of exothermic chemistry instead of a strong heating efficiency accounts for the heating due to the solar EUV while producing comparable temperatures to empirical models. V-GITM neutral temperatures and neutral-ion densities are compared to upper atmosphere measurements obtained from Pioneer Venus and Venus Express. V-GITM demonstrates asymmetric horizontal wind velocities through the cloud tops to the middle thermosphere and explains the mechanisms for sustaining the wind structure. In addition, V-GITM produces reasonable dayside ion densities and shows that the neutral winds can carry the ions to the nightside via an experiment advecting O_2^+.

Corresponding author: B. M. Ponder, bponder@umich.edu

Key Points:

- A new, non-hydrostatic Venus ionosphere-thermosphere model is introduced with new physics not previously included in Venus GCMs.
- Simulations during solar minimum conditions are used for data-model comparisons of the temperatures, plasma and neutral densities.
- The influence of the retrograde superrotating zonal flow is explored in relation to how it affects the neutral temperature and velocities.

Plain Language Summary

A state-of-the-art Venus global circulation model is being presented. The new model, V-GITM, has implications for usefulness in answering unknown questions about Venus' atmosphere, the physics of CO_2 rich planets, and Venus missions utilizing the aerobraking maneuver, like VERITAS or DAVINCI. Many V-GITM simulations were performed and the results were compared to some of the existing Venus datasets to assess the accuracy of V-GITM. Furthermore, the cloud layer below the thermosphere has a unique wind pattern and its impact on the thermosphere temperatures and winds were explored. Also, some of the driving mechanisms necessary for creating a nightside ionosphere at Venus were examined.

1 Introduction

The search for life in our galaxy is a fundamental quest. In order to help in this process, an understanding of the habitability of different planetary environments is important. The launch of the new James Webb Space Telescope with the Transiting Expolanet Survery Satellite (TESS) will bring new data from the mapping of transiting exoplanets around bright stars, allowing spectroscopic analysis of a planet's atmospheric composition. Planets that are very close to the star are more likely to be observed due to the higher frequency of passing in front of the star. Along with this, there are characteristics that inner, rocky exoplanets may have in common. For example, it has been found is that the closer planets are to a star, the more likely they are to be tidally locked [*Barnes*, 2017]. In addition, planets near a star often times encounter large amounts of solar radiation leading to the escape of lighter species, such as hydrogen and oxygen, throwing the carbon cycle out of balance resulting in a CO_2 rich atmosphere [*Ehrenreich, D. and Désert, J.-M.*, 2011] [*Taylor, F.W. et al.*, 2018]. In our own solar system, Venus shares some of these characteristics. For example, Venus is not tidally

locked, but has a very slow axial rotation period of 243 days which may respond similarly to the effects of stellar heating of tidally locked planets.

Further, Venus' atmosphere is dominated by CO_2. Comparative planetology of terrestrial planets and the role of CO_2 15 μm cooling in regulating the temperature structure of their upper atmospheres has been shown to be different between Venus, Earth and Mars [*Bougher et al.*, 1999]. As such, the CO_2 rich planets (Mars and Venus) have much colder thermospheric temperatures than at Earth. Knowing that radiative cooling is such an important process for these planets and is so dependent on atomic O and CO_2 densities, it becomes equally important to constrain the densities of each species. As pointed out in *Huestis et al.* [2008], atomic O should have variability throughout the solar cycle for Mars and Venus but measurements are severely lacking. *Bougher et al.* [2023] used MAVEN NGIMS datasets and compared to M-GITM simulations to capture solar cycle effects upon exospheric temperatures. Measured O abundances were used to constrain simulated O densities and CO_2 cooling rates on Mars for the first time.

Atmospheres dominated by CO_2, slowly-rotating and tidally locked planets are very different than what we experience at Earth, but may be commonplace in exoplanets. For example, over 5,200 confirmed exoplanets are cataloged in NASA's Exoplanet Archive. A good way to partition whether they are potentially habitable is to link Venus-like or Earth-like characteristics for each exoplanet.

Measurements and numerical models are used to answer questions about the evolution, habitability, and the underlying physics of these atmospheres. Models allow for testing of different configurations, characterizing uncertainty ranges to broadly predicting habitability. On the other hand, direct measurements are probably the most reliable sources of data to attempt to improve our understanding of these atmospheres, but obtaining this data is a difficult task, and therefore the measurements are quite limited. New missions and modeling efforts characterizing the dynamics of the atmospheres of Venus and Mars assist in understanding atomic O densities and the radiative cooling that results. As our ability to describe the role of radiative cooling at Venus and Mars improves, we will be able to better synthesize exoplanet data and improve our ability to assess the habitability of planetary bodies.

1.1 Venus Data Sets used for Comparison in This Work

A variety of satellite missions with different instruments have visited Venus to collect data on the atmospheric state. Ground-based telescopes (see James Clark Maxwell Telescope and Heinrich Hertz Submillimeter Telescope) are capable of mesospheric temperatures and carbon monoxide densities. Remote-sensing revealed the temperatures at a larger variety of altitudes and the atmosphere's neutral and ion densities. *Limaye et al.* [2017] has compiled many ground-based and satellite-based instrument measurements of Venus' atmosphere and ionosphere, which are summarized here, and used in later sections to validate model results:

- SPICAV (Spectroscopy for the Investigation of the Characteristics of the Atmosphere of Venus) uses a UV spectrometer and two IR spectrometers onboard Venus Express [*Bertaux et al.*, 2007]. The UV instrument provides density and temperature profiles from approximately 60 km to 160 km. The VIS-IR instrument is one of two infrared sensors, but this is used in the $0.7 - 1.7 \mu m$ wavelength range to gather H_2O, CO_2 and aerosol information along with $O_2(1 \quad - \quad \Delta)$ nightglow. SOIR (solar occultation IR) is part of the SPICAV suite of spectrometers, but measures CO_2 spectral lines from 2.2-4.3 μm [*Korablev et al.*, 2003], [*Mahieux et al.*, 2008]. Data is available at a wide variety of latitudes at the terminators between 70-170 km.
- JCMT (James Clark Maxwell Telescope) is a ground-based radio telescope in Hawaii that is capable of making sub-mm observations of CO absorption lines and temperatures between 70-110 km. Due to the differences in day-night CO densities, the observation range may vary.
- HHSMT (Heinrich Hertz Sub-Millimeter Radio Telescope) is located at the Arizona Radio Observatory and provides temperature profiles and CO distributions from 40-120 km on the dayside and nightside [*Rengel et al.*, 2008].
- VeRa (Venus Express Radio Science) used radio signals to sound Venus' atmosphere and ionosphere at all longitudes and latitudes during Venus atmospheric occultation (i.e., the signal is occulted by Venus's atmosphere). During the occultations, Venus' atmosphere lies between satellites radio transmitter and the ground station receivers or on Deep Space Network antennas. Measurements of the attenuated radio signals were used to derive atmospheric states. VeRa.0 and VeRa.1 provide density and temperatures from 40 km up to roughly 100 km [*Häusler et al.*, 2006].

- VIRTIS-H (Visible and InfraRed Thermal Imaging Spectrometer, high resolution channel) observed non-LTE emissions of carbon monoxide as part of the Venus Express spacecraft. *Gilli et al.* [2015] retrieved dayside temperatures, albeit with large uncertainties, between 100-150 km at a variety of local time and latitude bins by averaging non-LTE emission measurements.
- Pioneer Venus' Orbiter Neutral Mass Spectrometer (ONMS) measured density variations at low latitudes in the upper thermosphere [*Keating et al.*, 1979]. The data observed from this instrument are the foundation for the VTS3 empirical model, which is discussed more in the next section.

In addition to the data currently available, there have been two recently selected missions, VERITAS and DAVINCI, which will probe the atmosphere of Venus with new instruments. Venus Emissivity, Radio Science, InSAR, Topography, and Spectroscopy (VERITAS) aims to improve upon the radar maps from the Magellan mission in the 1990s, help scientists learn about the nightside IR emissivity, and measure the gravitational field around Venus to gain insights on the planet's core. VERITAS, now optimistically scheduled to launch in 2031, will perform aerobraking maneuvers that will sample the thermosphere and provide further constraints on upper atmospheric structure. The Deep Atmosphere Venus Investigation of Noble gases, Chemistry, and Imaging (DAVINCI) mission is planned to launch as early as 2029. DAVINCI aims to deliver high precision measurements of the composition of the atmosphere as it descends through the thermosphere down to near surface altitudes [*Garvin et al.*, 2022].

Piecing together all the data provides clues about the composition, dynamics and energetics of Venus' atmosphere, but they only tell part of the story due to data being available at limited times and discrete locations. Models are tools that can provide a complete four-dimensional dataset and can test our understanding of the physics of the Venusian atmosphere. Models have a variety of structures and assumptions that shape their usefulness in different situations.

1.2 Model Review

There are many models (empirical and first-principles-based) of the Venusian thermosphere:

- VTS-3: An empirical model created by *Hedin et al.* [1983] that used a spherical harmonic fitting of measurements from Pioneer Venus' Orbiter Neutral Mass Spectrometer (ONMS) from 1978 - 1980 to estimate measurements from 100 km to around 300 km. Near equator sampling by ONMS do not provide VTS-3 with useful mid-to-high latitude constraints. Also, ONMS in-situ datasets did not make measurements below about 140 km so extrapolations down to 100 km by VTS-3 are not well constrained. Empirical models rely on data assimilation from remote observations so they are able to estimate background atmospheric states well, but due to low statistics do not have the same success in dynamic conditions, such as flares. VTS-3 is used as a comparison tool for the model presented here.
- The empirical model from *Theis et al.* [1984] and *Theis and Brace* [1993] provide electron densities and electron temperatures extracted from Pioneer Venus' Orbiter Electron Temperature Probe (OETP) using the method described in *Krehbiel et al.* [1980]. This has similar latitudinal and altitudinal constraints as VTS-3.
- VIRA (Venus International Reference Atmosphere) used both lower and upper atmosphere datasets to capture reference profiles at specific locations and intervals throughout the solar cycle [*Kliore et al.*, 1985]. For instance, upper atmospheric mass densities and temperatures were based upon PVO OAD datasets [*Keating et al.*, 1985]. VIRA-2 [*Moroz and Zasova*, 1997] updated the reference profiles based on composition, temperature and pressure measurements.
- VTGCM: The Thermosphere Ionosphere General Circulation Model (TIGCM) [*Dickinson et al.*, 1984] was modified to work at Venus [*Bougher et al.*, 1988, *Brecht et al.*, 2011, 2012, *Parkinson et al.*, 2021]. VTGCM is a 3D physics-based model on a pressure coordinate system. At the time, this model displayed the importance of 15 μm CO_2 cooling to balance EUV heating effects. VTGCM also uses a wave-drag parameterization to reduce the horizontal wind speeds.
- V-PCM: The Laboratoire de Météorologie Dynamique (LMD) team created a Venus GCM, formerly LMD-VGCM, [*Gilli et al.*, 2017, 2021, *Navarro et al.*, 2021, *Martinez et al.*, 2023] now referred to as the Venus Planetary Climate Model (V-PCM). The V-PCM includes two unique parameterizations for the effects of the near IR solar heating at 4.3 μm and the radiative cooling at 15 μm. Additionally, a gravity wave parameterization is included to dampen the fast winds and improve stability of runs.

- TUGCM: Tohoku University's GCM (TUGCM) [*Hoshino et al.*, 2012, 2013] uses an atmosphere of O, CO and CO_2 only and implements planetary scale waves (Rossby waves, diurnal and semidiurnal tides, and Kelvin waves) based on the assumption that these are driven upward from the mesosphere.

A side-by-side comparison of the physics-based models (V-PCM, TUGCM and VT-GCM) was put together in *Martinez et al.* [2021]. This comparison table presents some features of each model and was modified to justify the development of a new model, V-GITM. Table 1 shows the high-level differences between each model.

	V-GITM	**VTGCM**	**V-PCM**	**TUGCM**
State variables	T, u, v, w, p, see Table 2 for neutrals and ions considered	T, u, v, w, O, CO, N_2, CO_2, Z, N(^{4}S), N(^{2}D), NO, O_2, SO, SO_2, PCE ions	T, u, v, w, O, CO, CO_2 + photochemical model [*Stolzenbach et al.*, 2023]	T, u, v, w, O, CO, CO_2, N, Z
Vertical domain	70-170 km: 1 km spacing	70-200/300 km: 69 pressure levels	0-200/250 km: 90 pressure levels	80-150/180 km: 38 pressure levels
Horizontal Resolution (Lon × Lat)	Flexible, in this work $5^\circ \times 2^\circ$	$5^\circ \times 5^\circ$	$3.75^\circ \times 1.875^\circ$	$10^\circ \times 5^\circ$
Temporal discretization	Runge-Kutta Fourth Order, 0.5-1s timestep	Leapfrog scheme, 20s timestep	Leapfrog-Matsuno scheme, 21s timestep	Leapfrog scheme, 4s timestep
Hydrostatic assumption	No	Yes	Yes	Yes
Ionosphere	Photochemistry and O_2^+ dynamics	Photochemistry	Photochemistry	-
EUV Heating	Chemical heating + 1% FISM model	20-22% F10.7 model	17% E10.7 model	10% F10.7 model
Near IR	Direct absorption with an IR heating efficiency	Tabulated heating rates from: *Roldán et al.* [2000] *Crisp* [1986]	*Martinez et al.* [2023]	Ratios between NLTE and LTE heating rates calculated by the GCM [*López-Valverde et al.*, 1998]
Eddy diffusion coefficient ($m^2\ s^{-1}$)	300	10-1000 Max value occurs above turbopause	-	0-500 Max value occurs above turbopause

Table 1. Four physics-based Venus models side-by-side comparing model characteristics and physics parameterizations. Adapted from *Martinez et al.* [2021].

1.3 The Need for a New Venus Model

This study introduces a new Venus model which is focused on better understanding (1) how the nightside ionosphere of Venus is sustained, (2) what controls the thermospheric temperature as a function of altitude and solar zenith angle, (3) the impact of the retrograde super-rotating flow on the winds, densities, and temperatures, and (4) the role of the wind dynamics on day-night structures. The flexibility in the new model improves upon the simulated physics and leads to better answering the outstanding questions at Venus. The three important improvements to the physics this work offers are the use of chemical heating, a non-hydrostatic solver and the inclusion of coupled ion dynamics.

For example, the method of using chemical heating is standard at Earth, but less common for planetary environments. It is typical for GCMs to adopt a heating efficiency to account for the heating effects from the solar EUV. In many cases, this method offers a good approximation, but the implementations are incomplete when using a uniform heating efficiency due to the solar EUV heating coming through a route of ionizing neutrals that release heat in exothermic chemical reactions. Ions are not uniformly distributed and so the chemical reactions do not heat the thermosphere uniformly making a constant heating efficiency inaccurate. The use of an uncertain heating efficiency produces an unreliable heating balance which may simulate incorrect temperatures and wind speeds or, in the case of plausible results, it biases our understanding of the physics incorrectly.

Hydrostatic equilibrium is a state of planetary atmospheres when the vertical pressure gradients are balanced by the effects of the planet's gravitational pull. This balance prevents atmospheres from being completely lost to space or collapsing under its own weight. As shown in Table 1, the existing Venus GCMs assume hydrostatic equilibrium to simplify the vertical wind calculation. V-GITM's non-hydrostatic solver is better-suited to address questions at Venus where it is still undetermined if the hydrostatic assumption is always appropriate. The hydrostatic assumption breaks down when vertical and horizontal scales are on the same order of magnitude, which is not the case in this study, but become more important as finer resolutions are used. *Navarro et al.* [2021] began exploring the effects of a finer horizontal grid and suggested the development of a shock on Venus. It was also mentioned that the hydrostatic dynamical core may be limiting the 3D modeling of shock formation. GITM explicitly solves for the winds without the use of artificial wave-breaking which is useful for allowing vertically propagating sound waves to form naturally. This makes V-

GITM a useful tool to support the findings of a shock-like feature or determine if the shocks are an artificial creation originating from the hydrostatic assumption.

Due to the slow-rotation of Venus, dayside ions do not co-rotate with Venus all the way to the nightside due to the timescales of chemistry. For this reason, Venus' nighttime ionosphere is assumed to be driven by ion dynamics or precipitating particles. Currently, VTGCM and V-PCM assume use a chemistry model with no advection to simulate the ionosphere. As discussed in section 2.3, V-GITM includes the dynamics of O_2^+ in an attempt to create a nightside ionosphere.

2 The Venus Global Ionosphere-Thermosphere Model (V-GITM)

The original Global Ionosphere Thermosphere Code [*Ridley et al.*, 2006] was adapted into a Mars model that goes from the surface of Mars to 300 km which has been referred to as M-GITM [*Bougher et al.*, 2015]. M-GITM is a 3D spherical code based in altitude coordinates that solves the Navier Stokes equations for the ions, electrons, neutral densities, temperatures and winds as well as the ion composition and velocities. It includes multiple parameterization models that are embedded in the code, including: (1) a model to simulate the effects of the dust in the lower atmosphere of Mars [*Jain et al.*, 2020]; (2) a modern NLTE CO_2 15 μm cooling scheme [*Roeten et al.*, 2019] and (3) a FISM-M solar flux model, based upon MAVEN EUVM measured EUV-UV fluxes at Mars, is used to drive M-GITM solar heating, dissociation and ionization rates [*Thiemann et al.*, 2017]. A flat 20% EUV heating efficiency is used. FISM is able to better represent the solar EUV entering the Martian atmosphere compared to an Earth-based F10.7 proxy model.

V-GITM begins with the Mars GITM code, taking advantage of existing chemistry and CO_2 cooling scheme. Mars unique processes, such as dust storms and wave-drag parameterizations, are removed in the new model. The solar EUV heating has transitioned from using a 20% heating efficiency to primarily using chemical heating.

2.1 Planetary and Orbit Characteristics

The GITM code is very modular, making updating planet and orbit characteristics straightforward to update. Some of the main items that required updating are shown in Table 1.

Property	Mars	Venus
Surface Gravity (m/s^2)	3.73	8.87
Rotation period (days)	1.03	233.5
Radius (km)	3388.25	6051.8
Axial Tilt	25.19°	0°[1]
Sun-Planet Distance (AU)	1.38-1.67	0.718-0.728
Eccentricity	0.093	0.0067
Neutral Species Considered	$\mathbf{CO_2}$, $\mathbf{CO}$, $\mathbf{N_2}$, $\mathbf{O_2}$, $\mathbf{O}$, $\mathbf{Ar}$, $\mathbf{N(^4S)}$, $\mathbf{He}$	$\mathbf{CO_2}$, $\mathbf{CO}$, $\mathbf{N_2}$, $\mathbf{O_2}$, $\mathbf{O}$, $\mathbf{N(^2D)}$, $\mathbf{Ar}$, $N(^4S)$, NO
Ion Species Considered	O_2^+, O^+, CO_2^+, N_2^+, NO^+	$\mathbf{O_2^+}$, $\mathbf{O^+}$, CO_2^+, N_2^+, NO^+

Table 2. Planetary constants used for M-GITM and V-GITM. In the case of the final two constants related to orbit characteristics, these values come from *Bannister* [2001] that have compiled tables from NASA JPL's website (http://ssd.jpl.nasa.gov/). Bolded ion/neutral species are advected in the model. [1]Venus' true axial tilt is around 3°, flipped for retrograde rotation. 0° is used as an approximation until the retrograde rotation is added.

2.2 Neutral Dynamics

V-GITM is developed based on the the Earth and Mars Global Ionosphere Thermosphere Models with its own unique set of atmosphere species considered (Table 2). The atmospheric constituents and resulting chemistry are very similar to Mars with CO_2 being the major species getting overtaken in the upper thermosphere by atomic oxygen. The model solves the continuity, momentum and temperature equations in three dimensions using a finite difference scheme without assuming hydrostatic equilibrium. The GITM frameworks splits the horizontal solver, vertical solver, and source terms. Below, the vertical equations with source terms are described in detail, while the horizontal advection equations are similar to those described in *Ridley et al.* [2006].

The continuity equation is:

$$\frac{\partial N_s}{\partial t} + \frac{\partial u_{r,s}}{\partial r} + \frac{2u_{r,s}}{r} + u_{r,s}\frac{\partial N_s}{\partial r} = \frac{1}{N_s}C_s \tag{1}$$

where r is the radial (vertical, positive outward) direction in spherical coordinates, N_s is the total number density for species s for each bolded element in Table 2 , C_s is the sum of the source and loss terms due to chemistry and $u_{r,s}$ is the vertical velocities of species s. The sources and losses due to chemistry are computed for the reactions in Table 3.

Photolysis is the category of reactions that are performed when incoming radiation causes an ionization or dissociation of a neutral particle. This is a necessary component for creating and maintaining the dayside ionosphere on Venus. When ions are created, they may undergo charge exchange or recombination with an electron. Charge exchange or recombination are typically exothermic reactions and therefore produce heat that gets absorbed in the atmosphere. Keeping track of this exothermic chemical heating is a major difference in V-GITM from existing Venus models that approximate this process via a direct heating rate, taking a fixed percentage (typically between 8-25%) of the incoming solar EUV energy deposition and using that as an energy source.

Reaction Number	**Chemical Reaction**	**Reaction Rate** ($m^3 s^{-1}$)	**Exothermicity** (eV)
Photolysis			
R1	$N_2 + h\nu \rightarrow N(^4S) + N(^2D)$		
R2	$N_2 + h\nu \rightarrow N_2^+$		
R3	$CO_2 + h\nu \rightarrow CO_2^+$		
R4	$CO_2 + h\nu \rightarrow CO + O$		
R5	$O + h\nu \rightarrow O^+$		
R6	$O_2 + h\nu \rightarrow 2O$		
R7	$O_2 + h\nu \rightarrow O_2^+$		
R6	$NO + h\nu \rightarrow N(^4S) + O$		
R7	$NO + h\nu \rightarrow NO^+$		
Neutral Bimolecular Chemistry			
R8	$CO_2^+ + O \rightarrow O_2^+ + CO$	1.64×10^{-16}	1.33
R9	$CO_2^+ + O \rightarrow O^+ + CO_2$	9.6×10^{-17}	-
R10	$CO_2 + O^+ \rightarrow O_2^+ + CO$	1.1×10^{-15}	1.21
R11	$N(^4S) + O \rightarrow NO$	See Appendix A	-
R12	$N(^2D) + O \rightarrow N(^4S) + O(^3P)$	2.0×10^{-17}	2.38
R13	$N(^2D) + O \rightarrow N(^4S) + O(^1D)$		0.42
R14	$N(^2D) + CO_2 \rightarrow NO + CO$	2.8×10^{-19}	-
R15	$O_2^+ + N(^4S) \rightarrow NO^+ + O$	1.0×10^{-16}	4.19
R16	$O_2^+ + N(^2D) \rightarrow NO^+ + O$	1.8×10^{-16}	-
R17	$O_2^+ + NO \rightarrow NO^+ + O_2$	4.5×10^{-16}	2.81
R18	$O_2^+ + N_2 \rightarrow NO^+ + NO$	1.0×10^{-16}	-
R19	$N_2^+ + CO_2 \rightarrow N_2 + CO_2^+$	$9.0 \times 10^{-16}(300/T_i)^{0.23}$	1.81
R20	$N_2^+ + O_2 \rightarrow N_2 + O_2^+$	$5.1 \times 10^{-17}(300/T_i)^{1.16}$	3.5
R21	$N_2^+ + O \rightarrow NO^+ + N(^2D)$	See Appendix A	3.06
R22	$N_2^+ + O \rightarrow O^+ + N_2$	$7.0 \times 10^{-18}(300/T_i)^{0.23}$	1.01
R23	$N_2^+ + NO \rightarrow N_2 + NO^+$	3.6×10^{-16}	6.32

277 **Table 3.** Photolysis and neutral bimolecular chemistry reactions with their corresponding reaction rates and
278 exothermicity in V-GITM. Reaction rates are adopted from [*Fox and Sung*, 2001].

Reaction Number	**Chemical Reaction**	**Reaction Rate** ($m^3 s^{-1}$)	**Exothermicity** (eV)
Electron Recombination Chemistry			
R24	$O_2^+ + e \rightarrow O(^3P) + O(^3P)$	$2.4 \times 10^{-13}(300/T_e)^{0.7}$	6.99
	$\rightarrow O(^1D) + O(^3P)$		5.02
	$\rightarrow O(^1D) + O(^1D)$		3.06
	$\rightarrow O(^1D) + O(^1S)$		0.83
R25	$CO_2^+ + e \rightarrow CO(X^1\Sigma^+) + O(^3P)$	$3.5 \times 10^{-13}(300/T_e)^{0.5}$	8.31
	$\rightarrow CO(a^3\Pi) + O(^3P)$		2.3
	$\rightarrow CO(a'^3\Sigma^+) + O(^3P)$		1.26
	$\rightarrow CO(d^3\Delta) + O(^3P)$		0.49
R26	$NO^+ + e \rightarrow O + N(^4S)$	$3.0 \times 10^{-13}\sqrt{300/T_e}$	2.75
	$\rightarrow O + N(^2D)$	$1.0 \times 10^{-13}\sqrt{300/T_e}$	0.38
R27	$N_2^+ + e \rightarrow 2N(^2D)$	See Appendix A	1.06
Termolecular Neutral Chemistry			
R28	$O + CO + CO_2 \rightarrow 2CO_2$	$6.5 \times 10^{-45} e^{-2180/T_n}$	-
R29	$O + O + CO_2 \rightarrow O_2 + CO_2$	2.75×10^{-44}	-
R30	$O + O + CO \rightarrow CO_2 + O$	$3.4 \times 10^{-39} e^{-2180/T_n}$	-
R31	$O + CO + CO \rightarrow CO_2 + CO$	$6.5 \times 10^{-39} e^{-2180/T_n}$	-

Table 4. Electron recombination and termolecular neutral chemistry reaction rates and exothermicity in V-GITM. Reaction rates are adopted from [*Fox and Sung*, 2001].

During O_2^+ and CO_2^+ recombination, many different states of O and CO can be produced. V-GITM groups all excitation states as one species in the model, i.e. $O(^1D)$, $O(^3P)$, and $O(^1S)$ are handled as just O. The same is done for CO's different states. The branching ratios that describe the partitioning into each state is important due to the different exothermicity associated with each recombination. Regarding CO_2^+ recombination (see R25), the branching ratios used are (0.24, 0.38, 0.18, 0.20) as follows from *Rosati et al.* [2003] and *Gu et al.* [2020].

O_2^+ recombination (see R24) branching ratios also vary with the O_2^+'s vibrational state (ν). As described in *Petrignani et al.* [2005], the branching ratio for $\nu = 0$ is (0.265, 0.473, 0.204, 0.058), $\nu = 1$ is (0.073, 0.278, 0.51, 0.139), and $\nu = 2$ is (0.02, 0.764, 0.025, 0.211). To approximate the correct fractional population of the vibration states by altitude, Figure 1 in *Fox* [1985] was followed. Below 130 km the vibrational population of O_2^+ is assumed to be 100% in the $\nu = 0$ state. In the altitude range of 130 km - 170 km, each vibrational state was interpolated between the fractional population values found at 130 and 170 km.

At the bottom boundary, each neutral species density is fixed using a constant value estimated by VTS3 except O, N(^{4}S), N(^{2}D), and NO which are all zero. The top boundary assumes a hydrostatic fall off of each species number density.

The vertical momentum equation is:

$$\begin{aligned} \frac{\partial u_{r,s}}{\partial t} + u_{r,s}\frac{\partial u_{r,s}}{\partial r} + \frac{u_\theta}{r}\frac{\partial u_{r,s}}{\partial \theta} + \frac{u_\phi}{r\cos(\theta)}\frac{\partial u_{r,s}}{\partial \phi} \\ + \frac{k}{M_s}\frac{\partial T}{\partial r} + T\frac{k}{M_s}\frac{\partial N_s}{\partial r} \\ = g + F_s + \frac{u_\theta^2 + u_\phi^2}{r} + \cos^2(\theta)\Omega^2 r + 2\cos(\theta)\Omega u_\phi \end{aligned} \tag{2}$$

where the north latitude direction is θ and the east longitude direction is ϕ. The eastward and northward bulk velocities are u_ϕ and u_θ, respectively. T is the neutral temperature, while M_s is the mass of species s. Venus' angular velocity and gravity are Ω and g respectively. The u_θ^2 + u_ϕ^2/r term is due to spherical geometry. The final two terms on the RHS are the centrifugal and Coriolis forces. Neutral-neutral and ion-neutral friction in the F_s are:

$$F_s = \frac{\rho_i}{\rho_s}\nu_{in}(v_r - u_{r,s}) + \frac{kT}{M_s}\sum_{q\neq s}\frac{N_q}{ND_{qs}}(u_{r,q} - u_{r,s}) \tag{3}$$

where ρ_i is the ion mass density, ν_{in} is the ion-neutral collision frequency, v_r is the ion velocity in the radial direction, N_q is the total number density for species q that species s interacts with, and N is the bulk number density. D_{qs} is the molecular diffusion coefficient between s and q species as described in *Colegrove et al.* [1966], table 1. $u_{r,q}$ is the vertical velocity of the other species s. Eddy vertical mixing is added to the vertical velocity solved for in Equation (2) at every time step. The eddy vertical velocity as shown in *Malhotra and Ridley* [2020]:

$$v^s_{eddy} = -K_{eddy}\frac{\partial}{\partial r}(ln(\frac{\rho_s}{\rho})) \tag{4}$$

where K_{eddy} is the eddy diffusion coefficient, ρ_s is the species-specific mass density, and ρ is the bulk mass density. Currently, the eddy diffusion coefficient used is a constant value of 300 m^2/s, but can be improved with future work following a variation of the non-uniform profile described in *Mahieux et al.* [2021]. 1D values of the eddy diffusion coefficient may be too large for 3D models, due to the global circulation serving to modify vertical density profiles, thereby reducing the need for additional turbulent effects added via an eddy diffusion coefficient [*Bougher et al.*, 1999].

The top boundary condition for the vertical winds is to have zero gradient for the out flow (positive radial velocities), while preventing any downflow (no downward radial velocities allowed). In the meridional (N/S) and zonal (E/W) direction, the top boundary conditions applies zero vertical gradient. The bottom boundary velocity is zero in the meridional direction and vertical direction, while the zonal velocity follows the cloud top behavior observed at Venus. The cloud motion is persistently westward and is commonly referred to as a retrograde superrotating zonal (RSZ) flow because it is faster than the rotation of the planet [*Bougher et al.*, 2008]. The lower boundary condition in the zonal direction is set to be -100 m/s with a cosine fall-off as a function of latitude as shown in Figure 1. This condition assists in better understanding the unique impact of the mesosphere on the thermosphere [*Peralta et al.*, 2017, *Schubert et al.*, 2007]. A cosine fall-off is an elementary approximation to capture the low-latitude zonal velocity while also reducing the observed high-latitude velocity, which rapidly dissipates poleward of 50-60° N/S [*Machado et al.*, 2012, 2017].

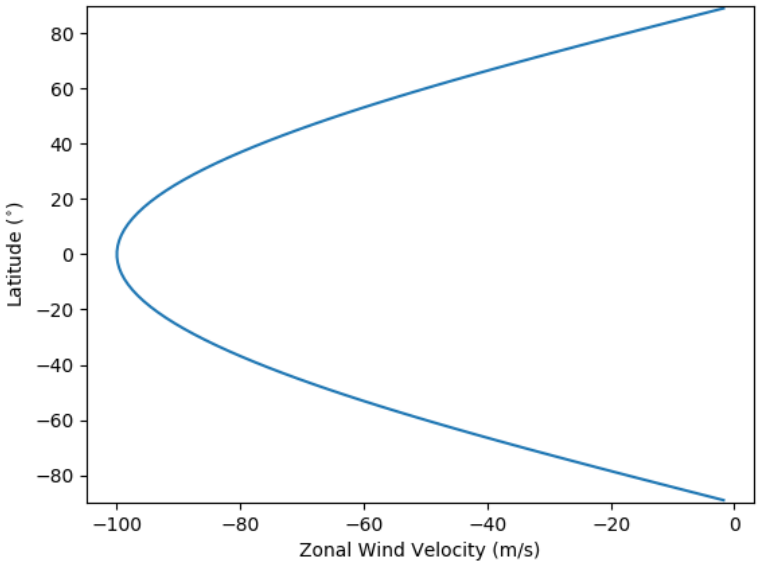

Figure 1. Zonal velocity lower boundary condition at 70 km altitude.

The vertical energy equation for the normalized, neutral temperature, $\mathcal{T} = kT/\bar{m}_n$ is:

$$\frac{\partial \mathcal{T}}{\partial t} + u_r \frac{\partial \mathcal{T}}{\partial r} + (\gamma - 1)\mathcal{T}\left(\frac{2u_r}{r} + \frac{\partial u_r}{\partial r}\right) = \frac{k}{c_v \rho \bar{m}_n} Q \tag{5}$$

where γ is the adiabatic index that is attached to the change in energy from the expansion of the gas, c_v is the specific heat constant, k is Boltzmann's constant, and $\bar{m}_n$ is the mean mass. The various source terms are given by:

$$Q = Q_{EUV} + Q_{IR} + Q_O + Q_{CO_2} + Q_{CHEM} + \frac{\partial}{\partial r}\left((\kappa_c + \kappa_{eddy})\frac{\partial T}{\partial r}\right) \tag{6}$$

where Q_{EUV} and Q_{IR} are the contribution from the Sun's extreme ultraviolet and infrared, respectively. The Q_O and Q_{CO_2} detail the cooling to space from the 63 μm and 15μm bands respectively. Q_{CHEM} combines heat generated from exothermic reactions. κ_{eddy} is the heat conductivity due to eddy diffusion coefficient and κ_c is the molecular heat conductivity.

There are multiple options for adding the EUV flux. One implementation is EUVAC [*Richards et al.*, 1994]. This model estimates the top of atmosphere flux in 37 wavelength bins based using the 10.7 cm solar radio flux. One issue with EUVAC is that it does not extend to long enough wavelengths to fully describe the CO_2 physics. Photoabsorption, photodissociation and photoionization cross-sections for these 37 bins can be

found in *Schunk and Nagy* [2004]. Another option is to use the Flare Irradiance Spectral Model (FISM) fluxes [*Chamberlin et al.*, 2008] which GITM re-bins into 59 wavelengths from 0.1 nm to 175 nm. This option allows the user to input their own top of atmosphere fluxes or absorption/ionization cross-sections. *Heays, A. N. et al.* [2017] has compiled more than 100 different atoms and molecular photoabsorption, dissociation and ionization cross-sections in 0.1 nm spacing. This data is stored in the Leiden Observatory database (`https://home.strw.leidenuniv.nl/~ewine/photo/`). The neutral gas heating efficiency, the fraction of the total EUV energy absorbed into the atmosphere directly, is computed using a flat 1%.

Due to the varying distance from the sun, the planets receive varying amounts of radiation. For Earth, the TIMED spacecraft's Solar EUV Experiment (SEE) instrument [*Woods et al.*, 2005] provides binned data for FISM. At Mars, the MAVEN satellite is able to monitor fluxes of several EUV wavelengths received at Mars [*Eparvier et al.*, 2015], allowing for a Mars-specific FISM [*Thiemann et al.*, 2017]. For V-GITM, the FISM values at Earth are used and then scaled according to the r^{-2} proportionality:

$$F_{venus} = F_{earth}(\frac{d_{se}}{d_{sv}})^2 \tag{7}$$

where F_{earth} is the FISM EUV fluxes observed at Earth, d_{se} is the distance between the sun and the Earth, d_{sv} is the distance between the sun and Venus. With using FISM fluxes from a non-Venus planet, it is somewhat difficult to determine how useful the scaled measurements are. These measurements are only sufficient assuming that Venus and Earth are on the same side of the sun during the time of the FISM measurements. Since the results presented here do not involve comparisons for specific intervals, it is assumed that this approximation is reasonable.

The source of near infrared heating is a complex process which involves solar radiation to be absorbed and excite a CO_2 molecule. De-excitation and heat deposition occurs via quenching, direct thermalization or transfer to other particles. IR wavelength bands between 2-4 μm. *Gilli et al.* [2017] created a parameterization based off of the non-LTE model heating rates produced from *Roldán et al.* [2000]. The parameterization was updated more recently in *Gilli et al.* [2021] to provide better agreement with the resulting PCM model's temperature structure. V-GITM can be run using either of these two parameterizations, but lacks IR heating at and beyond the terminators for the Gilli parameterization. For this reason,

the IR heating within V-GITM utilizes a similar method to the EUV absorption given a CO_2 absorption cross-section, top of atmosphere intensity and wavelength energy. The intensity is then attenuated as a function of the optical depth, which is computed using the constituents of the atmosphere's absorption coefficients and evaluating the Chapman integrals which help determine the optical path. Smith and Smith (1972) improved Chapman's accuracy at large solar zenith angles which better captures the solar EUV and IR heating effects near the terminators.

Although there are more processes than CO_2 absorption, a first-principles based method would require a full radiative transfer code which V-GITM does not have due to the complexity and extra computational expense. V-GITM attempts to follow *Gilli et al.* [2021]'s process of matching heating rates to temperature measurements. Instead of via a parameterization, CO_2 absorption at 2.7 μm and 4.3 μm with cross-sections prescribed at 6.5e-24 $m^2$and 3.0e-25 m^2 respectively. Top of atmosphere fluxes for the 2.7 and 4.3 μm were 1.25e-15 W/m^2 and 4.9e-16 W/m^2 respectively. Such small cross-sections deposit heat over a large altitude do6main which may not be representative of what is actually occurring and so an IR-specific heating efficiency is applied to reduce some of the heating in the non-LTE region. The heating efficiency shown in Figure 2 uses a flat 100% up to 135 km in which a cosine function is used to reduce the heating efficiency to 0% at 170 km. The cosine function used:

$$\epsilon_{IR} = \begin{cases} 1.0 & z \leq z_0, \\ \frac{1}{2}(\cos(\omega(z - z_0)) + 1) & z > z_0 \end{cases} \tag{8}$$

where z is the local altitude, z_0 is the altitude in which below 100% heating efficiency is applied (i.e. 135 km), and ω is the angular frequency to fit a half period between z_0 and the top of the model. In this case, $\omega = \pi/(z_{top} - z_0)$, where z_{top} is the top of model altitude. This is done because GITM's absorption-only scheme produces non-trivial heating effects at altitudes above 140 km where quenching and other effects occur that, while occuring at these wavelengths, would not be accurately modeled through absorption coefficients. The heating efficiency from equation (8) helps remove the higher altitude heating that would otherwise make this inconsistent with other estimations of the near IR heating [*Roldán et al.*, 2000, *Gilli et al.*, 2017, 2021].

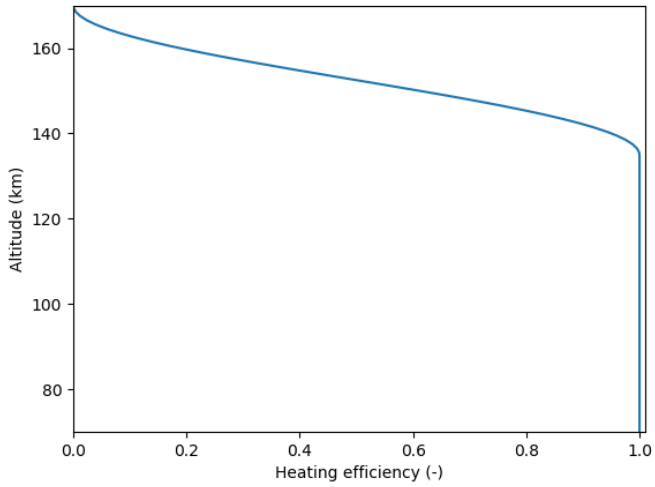

Figure 2. Infrared heating efficiency applied to direct absorption of 2.7 and 4.3 μm into CO_2.

The 15 μm cooling strongly controls the thermospheric structure at Venus [*Bougher et al.*, 1994, 1999]. Atomic oxygen excites CO_2 to enhanced vibrational and rotational states, which then radiates energy that is lost to space or is reabsorbed, depending on conditions. This process is responsible for the cold lower thermospheric temperature observed by satellite measurements [*Schubert et al.*, 1980, *Bougher et al.*, 1999, 2008]. To properly estimate the effects of the CO_2 cooling, a full radiative transfer model is best, but this is not computationally practical in 3D, so the cooling effects follow the M-PCM non-LTE paramaterization [*González-Galindo et al.*, 2013]. The non-LTE parameterization simplifies the full problem into 5 rotational and vibrational levels, computes heat transfer between atmospheric layers and allows for spatially variable atomic oxygen and CO_2 densities. This code has been used in the M-PCM, V-PCM and M-GITM models [*Bougher et al.*, 2017, *González-Galindo et al.*, 2013, *Gilli et al.*, 2017, 2021]. Due to the necessity of CO_2 cooling in the LTE portion of the thermosphere and the non-LTE nature of this model, the lower thermosphere is cooled using a linear extrapolation from approximately 70-95 km. The effects of this assumption are discussed in subsequent studies.

At the top of the model, the neutral temperatures has a zero gradient. The bottom boundary neutral temperature is fixed at 215 K motivated by *Limaye et al.* [2017]'s compiled datasets.

2.3 Ion Dynamics

The ion continuity equation is:

$$\frac{\partial N_i}{\partial t} + \frac{v_\theta}{r}\frac{\partial N_i}{\partial \theta} + \frac{v_\phi}{r\cos(\theta)}\frac{\partial N_i}{\partial \phi} + v_r\frac{\partial N_i}{\partial r} = S_i \tag{9}$$

where N_i is the number density of the i^{th} ion and S_i is net rate at which the i ion is being produced or lost. The bottom boundary has zero gradient for all ions, but does not matter due to lack of substantial ion densities at that altitude. At the top, the ion densities follow an exponential fall off.

The ion momentum equation in the Venus code is different than the equation found in *Ridley et al.* [2006]. The first difference is the removal of Lorentz force term due to the lack of planetary electromagnetic fields. The solver of the velocity is also changed due to the inclusion of the time rate of change term. The base ion momentum equation is:

$$\rho_i\frac{d\mathbf{v}}{dt} = -\nabla(P_i + P_e) + \rho_i\mathbf{g} - \rho_{\mathbf{i}}\nu_{\mathbf{in}}(\mathbf{v} - \mathbf{u}) \tag{10}$$

where the $\nabla(P_i + P_e)$ is the plasma pressure and $\mathbf{v}$ is the ion velocity. The velocity is solved for using an implicit time-stepping scheme, where the ion velocity on the right side of the equation is assumed to be the new velocity. The bottom boundary for the ion velocity is fixed at zero in the vertical direction. The top boundary has zero gradient for the horizontal drifts.

One of the problems with ionospheric models that are limited in altitude is that they can not capture the combined vertical and horizontal ion transport that may occur above the top of the model domain. For example, at Earth, ions flow up on the dayside into the plasmasphere, and then down at the night, filling in the nightside ionosphere. At Venus, there is evidence of O^+ transport at high altitudes from the dayside to the nightside during solar maximum to sustain the night-time ionosphere [*Kliore et al.*, 1979, *Knudsen*, 1992]. Currently, V-GITM does not advect O^+ and so it is not expected that the nightside ionosphere will be highly accurate yet.

During solar minimum, it is thought that the ionopause is compressed such that the ionosphere becomes too small to allow O+ transport to be the primary source of nightside ions, but rather that precipitating electron fluxes are sufficiently large to be a significant source of the ionization. *Kliore et al.* [1979] computed nightside electron densities from the precipitation of 30 eV, 75 eV, and 300 eV electrons based on information from Pioneer Venus measurements (figure 4 in their paper). *Theis and Brace* [1993] created an empirical

model that provides nightside electron density and electron temperature values also based on Pioneer Venus measurements, as shown in their Figure 3a. They showed the densities can vary by nearly an order of magnitude depending on the solar cycle. More work by *Brecht and Ledvina* [2021] showed a nightside electron density profile produced from a coupling of the VTGCM and HALFSHEL model which matches the results from *Theis and Brace* [1993]. No electron precipitation is included in V-GITM but it is something that could be implemented in future versions.

2.4 Initial Conditions and Model Domain

V-GITM follows the VTGCM model with an altitude range from 70 - 170 km. The smallest scale height, H is computed using the heaviest neutral species in the Venus atmosphere, CO_2. With a scale height of approximately 5 km, V-GITM's vertical grid is prescribed to be a uniform 1 km spacing. An adaptive time-step based on a CFL of 0.5 is used. The time-steps are typically 8-10 seconds for the $5^\circ \times 2.5^\circ$ (longitude $\times$ latitude) horizontal resolution used in this work.

The neutral densities are initialized using the VTS3 model, while the ion densities are all set to 1e-24 m^{-3} initially. Neutral and ion velocities are initialized to zero with a bottom boundary condition used to simulate a superrotating flow found near the cloud tops as described in Figure 1.

3 Simulation Results

In this section, the initial results of V-GITM simulations are shown for a run during March 1st-10th, 2009 in which the F10.7 was around 70 $Wm^{-2}Hz^{-1}$. This time period and F10.7 is representative of solar minimum conditions. Temperatures and densities as functions of time are shown to understand the necessary run-time for the model to reach an approximate steady state. The thermal structure, neutral and ion composition, and winds at the end of the run are shown with some accompanying data-model comparisons in Figures 3-17.

Figure 3 shows temperatures and densities at 75 km and 165 km for noon, midnight, dawn and dusk terminators. The noon and midnight quantities converge within three days with the exception of the 0 LT mass density at 165 km. Although temperatures (3a) and densities (3b) at the terminators changed throughout the entire run at 165 km, the variations are

very small compared to the mean values which implies that steady state conditions have been achieved within V-GITM. It is important to point out that although steady state is reached within 5 days, this is only applicable for the current state of V-GITM. Dynamical and chemical time scales determe the time to steady state. These time scales vary with altitude and are important to consider below 100 km, especially as additional chemistry is added to the model [*Brecht and Ledvina*, 2021].

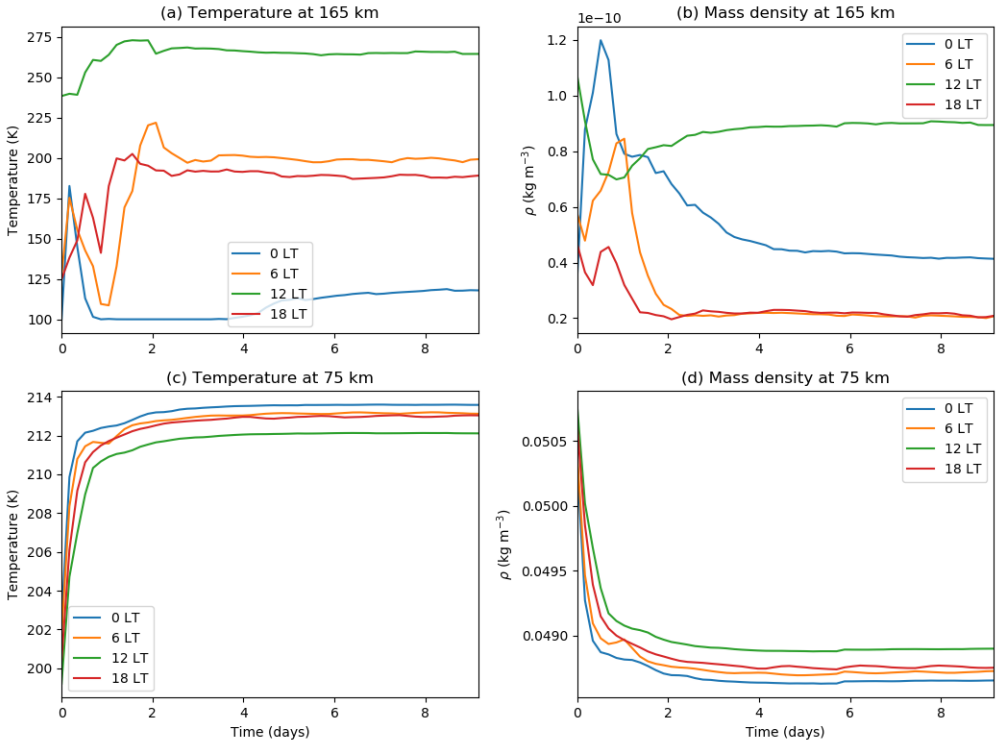

Figure 3. The mass density and neutral temperature as indicated near the equator for different local times at 165 km (panel (a) and (b)) and 75 km (panel (c) and (d)).

3.1 Thermal Balance and Structure

V-GITM's equatorial temperature as a function of longitude and altitude after 10 days of simulation time is shown in Figure 4. The lower altitudes do not have large source terms and the temperature fall off between 70 km to roughly 90 km stems from residual radiative cooling. Temperatures begin to increase above 90 km due to a contribution of heating from the solar near-IR that is absorbed by CO_2. On the dayside, the local temperature peaks at 215 K around 100 km because of the 2.7 μm and 4.3 μm contribution to the near IR heating.

Above this local maxima, temperatures decrease briefly until 120 km where the solar near IR absorption peaks and the 15 μm CO_2 cooling has a local minimum.

On the nightside near 0 LT, temperatures decrease from 70 km until 110 km where there is a temperature valley. Above this is a very small peak of around 200 K around 120 km. This temperature peak has significantly colder temperature, approximately 165 K, surrounding this location. The temperature island at midnight near 120 km is created due to fast winds converging on this location. These winds are generated by large pressure gradients stemming from the warm dayside. There is a warm temperature spot at 100 km as well, but a nighttime temperature peak is not observed because the wind pattern is significantly different from the wind pattern at 120 km. The causes of the different wind pattern is discussed more in section 3.3.1, but is primarily due to viscous interactions with the lower boundary that is significant up to 100 km, but is reduced by 120 km. As seen in Figure 4b, the horizontal winds are predominantly westward at 100 km which does not create compressional heating on the nightside.

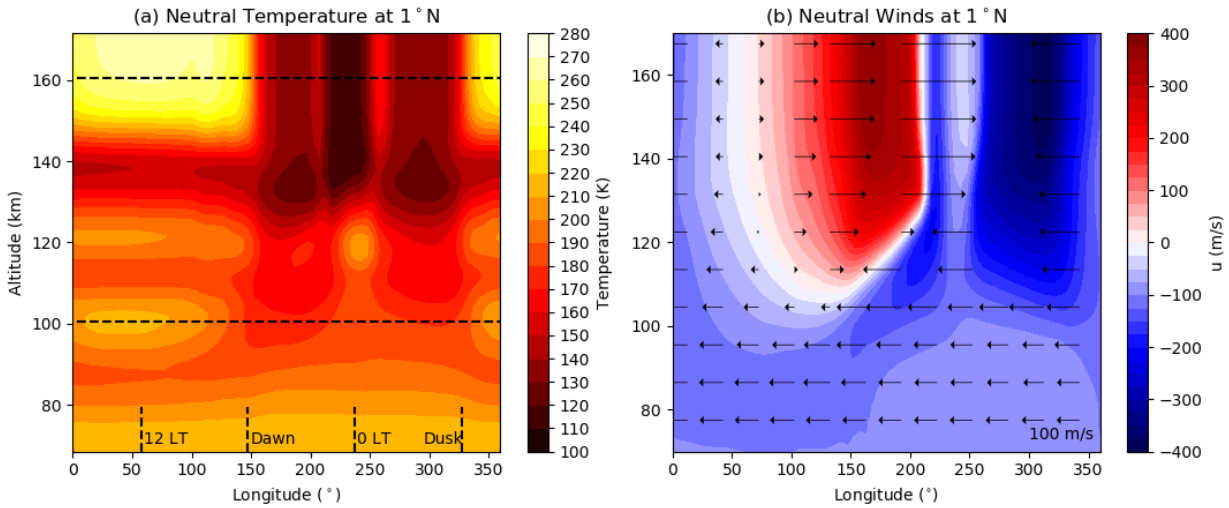

Figure 4. V-GITM temperature (left) and neutral winds (right) for a low solar activity simulation on March 10th, 2009 (F10.7 = 70) after simulating ten Earth days. Longitude-altitude cross-section taken at 1.0°N.

Above 140 km on the dayside, temperatures increase to an isothermal profile around 265 K. The heating is due to absorption of solar EUV in the form of direct heating and chemical heating. Between 140-170 km, the solar EUV is balanced by thermal conduction and CO_2 cooling. As shown in Figures 4 and 5, the diurnal variation is largest in this region

with day-night differences of approximately 150 K. The temperature differences drive pressure gradients that create fast winds in the upper thermosphere as shown in Figure 4b and discussed in section 3.3.

On the nightside, temperatures drop to 110 K at the top of the model because of the lack of heating sources, with the only source being from adiabatic heating at 200° and 260° longitude. As shown in Figure 5b, there is a ring where temperature increases due to the convergence of winds near midnight. This region is where the supersonic winds from the dayside to the nightside slow down to subsonic speeds. This behavior was shown in other modeling studies, such as *Navarro et al.* [2021]. This is discussed further in section 3.3.

Observational data from ground-based measurements from HHSMT and JCMT, along with Venus Express's VeRa data and empirical model results from VTS3 were compiled in *Limaye et al.* [2017]. Figure 6 shows a data-model comparison using the *Limaye et al.* [2017] data and V-GITM results (dashed black line) latitudinally binned from 30°S to 30°N and longitudinally binned based on local time (LT) between 7 LT and 17 LT.

Between 120 km and 135 km, there are limited measurements of the dayside temperature. Interpolating data from HHSMT at 120 km and VTS3 results at 135 km, it appears that temperatures should be between 180-200 K. HIPWAC-THIS and VIRTIS-H have measured this region with very large uncertainty bars. V-GITM's solar EUV quickly falls off below 145 km leading to a valley of temperature at 135-140 km. More measurements are needed to understand the appropriate heating and cooling balance in this region. This could be that solar EUV in V-GITM is not depositing energy low enough, the 2.7 μm near IR is not contributing at high enough altitudes, or some combination of the two.

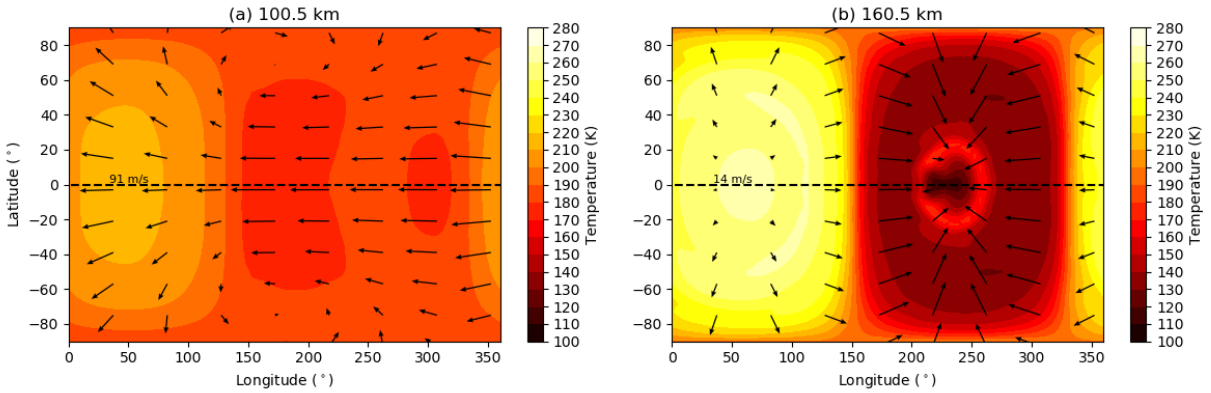

Figure 5. Temperature contours shown of constant altitude slices at (a) 100.5 km and (b) 160.5 km overlayed with horizontal winds for the same time as in Figure 4. A reference vector wind speed is shown at noon, near the equator, but maximum velocities are 137 m/s and 373 m/s for 100.5 km and 160.5 km, respectively.

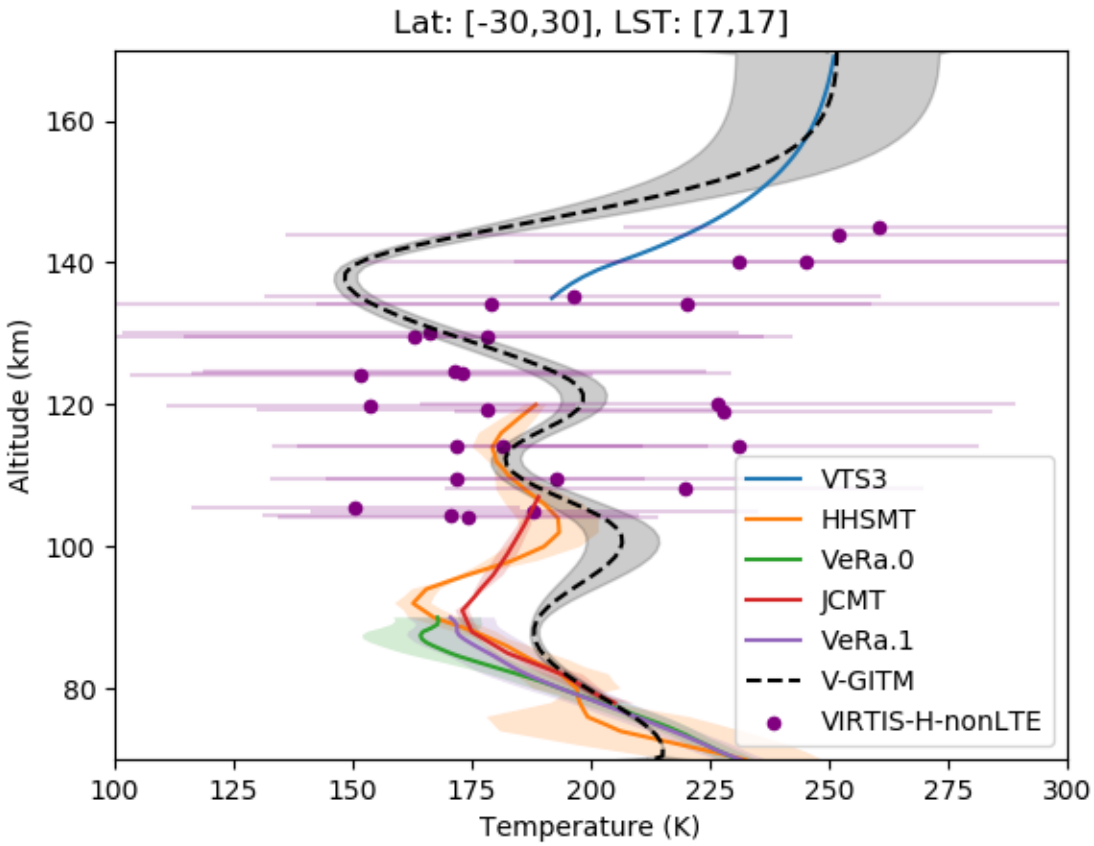

Figure 6. Dayside averaged temperature profiles from JCMT, HHSMT, VTS3, VeRa and V-GITM for the low latitude bins between -30° and 30° for March 10th, 00 UT, 2009. One standard deviation are plotted as colored areas for averaged profiles in the same bin.

The dayside heat balance described above is illustrated in Figure 7. The non-LTE 15 μm CO_2 cooling scheme is used between ~100 km-170 km. One correction that V-GITM includes is a linear extrapolation of NLTE CO_2 cooling value at 100 km value down to a desired 70 km cooling rate. This is due to a breakdown of the NLTE scheme which does not work effectively below 100 km. The extrapolation cooling scheme was chosen in an attempt to match the HHSMT, VeRa, and JCMT profiles.

The near IR heating rate is a the sum of contributions from the transmission and direct absorption of the 2.7 μm and 4.3 μm spectra. The 1D profile shown in Figure 7 features heating throughout a similar vertical domain as the parameterization of *Gilli et al.* [2017], but with a dayside peak heating rate similar to *Gilli et al.* [2021].

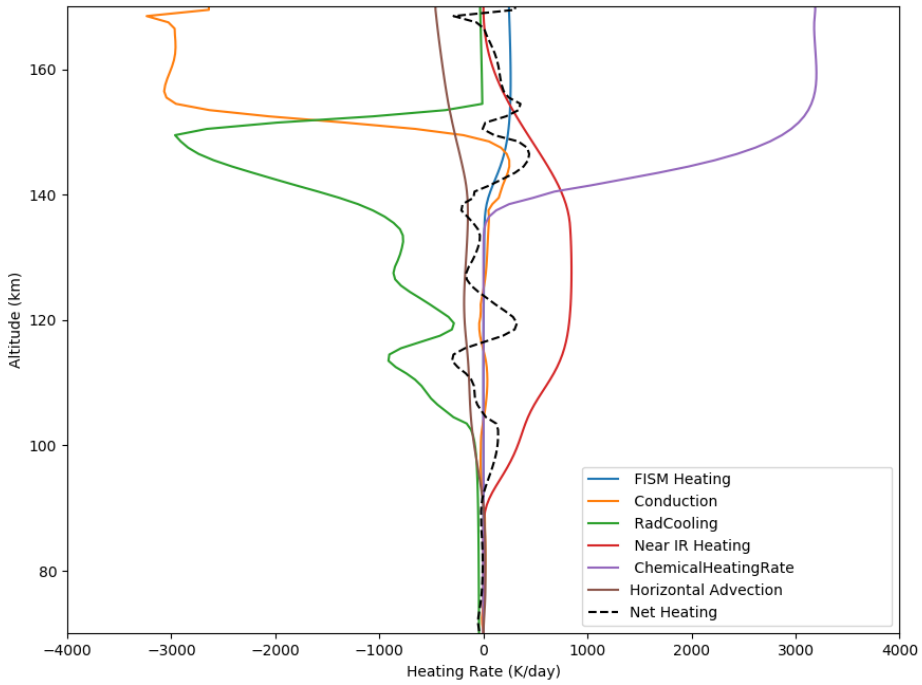

Figure 7. Heating and cooling rates (K/day) by V-GITM at 12 LT and 1°N for the same time as shown in Figure 4.

3.2 Neutral Densities

Resulting vertical profiles of V-GITM's nine individual neutral species from the simulation described above are shown in Figure 8. Several densities and density peaks are shown in Table 5 comparing the V-GITM results to VTS-3, Venus Express, VTGCM or *Fox and Sung* [2001]'s model.

Measurable Quantity	**V-GITM Result**	**Comparison Result**	**Reference**
$z(n_{CO_2} = n_O)$	165 km at 12 LT 140 km at 0 LT	165 km at 12 LT 140 km at 0 LT	VTS-3
$\max(n_{O,12LT})$	6×10^{10} cm^{-3}	-	-
$\max(n_{O,0LT})$	7×10^{11} cm^{-3}	2.5×10^{11} cm^{-3}	Venus Express [*Brecht et al.*, 2012]
n_N(140 km)	5.5×10^{7} cm^{-3}	3×10^{7} cm^{-3}	*Fox and Sung* [2001]
$n_{N(^2D)}$(140 km)	6.5×10^{4} cm^{-3}	2-3$\times10^{5}$ cm^{-3}	*Fox and Sung* [2001]
$z_{max}(n_{NO})$	95, 125 and 140 km	95 km	*Fox and Sung* [2001]
$\max(n_{NO})$	3.5×10^{6} cm^{-3}	2-3$\times10^{8}$ cm^{-3}	*Fox and Sung* [2001]
n_{CO}(170 km)	1.5×10^{8} cm^{-3}	1.2×10^{8} cm^{-3}	VTS-3
n_{N_2}(170 km)	1.4×10^{8} cm^{-3}	7.6×10^{7} cm^{-3}	VTS-3

Table 5. Notable density peak locations and number densities from V-GITM (see Figure 8) with a comparison against measurements or model-predicted results.

Atomic O overtakes CO_2 as the dominant species in the thermosphere at altitudes where molecular diffusion is stronger than eddy diffusion. Matching VTS-3, V-GITM showed this to occur on the dayside and nightside to occur near 165 km and 140 km, respectively. At midnight, V-GITM's atomic oxygen peak value is 7×10^{11} cm^{-3} at 120 km whereas Venus Express measured a smaller value of roughly 2.5×10^{11} cm^{-3} nearer 100 km [*Brecht et al.*, 2012]. The disparity between the nightside values at 100 km could be due to the westward winds at this altitude advecting oxygen to the nightside. The nightside O(1-Δ) airglow that results from this simulated O-density peak could be a useful constraint on the thermospheric circulation [*Brecht et al.*, 2011, 2012]. Although not done in this thesis, it is a topic of future work. Below 80 km, O has a rapid decreases in density due to the lower boundary condition. The lower thermosphere has not been reliably measured and so it is assumed that O will be completely depleted. Additionally, the dayside atomic oxygen density peak is smaller than the peak on the nightside. While it is unclear if this should be the case, having a dayside density to benchmark against is very important. Atomic oxygen is formed by CO_2 photodissociation on the dayside and advected to the nightside. Additionally, 15 μm cooling is highly dependent on oxygen densities. For these reasons, accurately constraining the dayside oxygen profile is necessary to improve the heat balance and nightside densities, chemistry and nightglow.

N and N(^2D) are also affected by the lower boundary condition to deplete them. N peaks at 3 $\times10^7$ cm^{-3} near 140 km as computed in *Fox and Sung* [2001] which V-GITM matches reasonably well. *Fox and Sung* [2001] suggests that the N density may fall off to nearly zero below 115 km which V-GITM does not reproduce. V-GITM shows a secondary peak at 95 km because the only N loss term acting at this altitude is R11 which is acts very slowly. N(^{2}D), on the other hand, should peak between 150 km with a magnitude around 2-3$\times10^5$ cm^{-3} from Fox's model. V-GITM showed the peak to be roughly a third of their value.

NO peaks near 95, 125 and 140 km in V-GITM. *Fox and Sung* [2001] shows that NO peaks near 95 km two orders of magnitude larger than that shown in V-GITM. Also pointed out in *Fox and Sung* [2001], NO below 120 km is created by N(^{2}D) and CO_2 producing NO and CO, balanced by a charge exchange between NO and O_2^+ to create NO^+. The N(^{2}D) density below 140 km is very small and so NO is not significantly produced. As seen in section 3.5, V-GITM has nearly no O_2^+ below 120 km preventing the charge exchange from

occurring. Further investigation in the chemical balance, particularly at lower altitudes, will be given to N, N(^2D) and NO in future work.

The CO and N_2 densities at 70 km and 170 km match the order of magnitude of those predicted via VTS3. As pointed out in *Mahieux et al.* [2021], CO and N_2 are chemically inactive, particularly at high altitudes in the atmosphere. Despite the mismatch in some of the individual profiles, the dayside total number density profile (Figure 9) has agreement throughout.

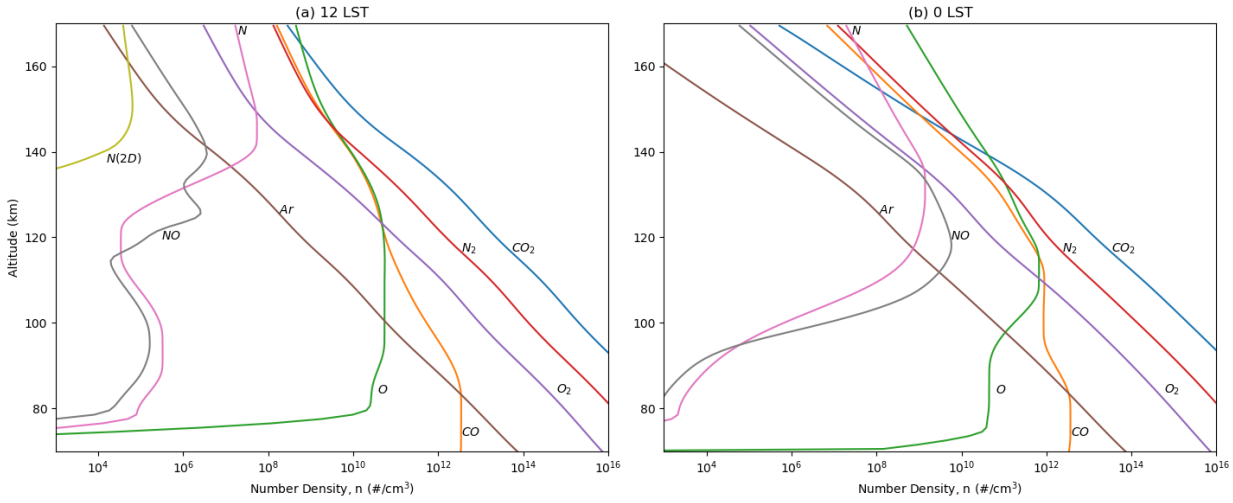

Figure 8. V-GITM altitude profile of neutrals at (a) 12 LST and (b) 0 LST at 1°N for March 10th 00:00:00 UT, 2009.

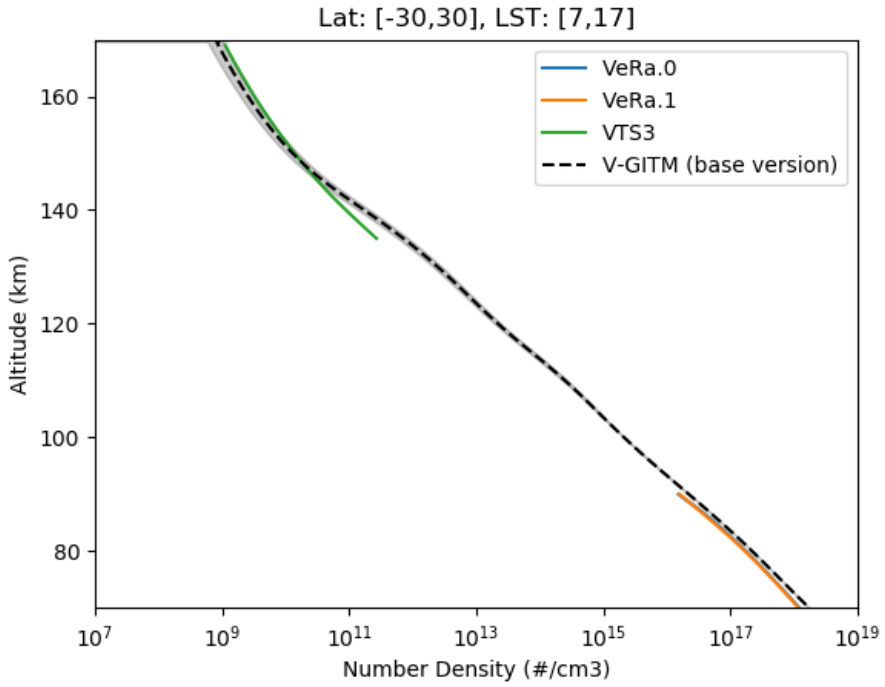

Figure 9. Dayside averaged from 30°S-30°N and from 7-17 LST density profiles from VeRa, VTS3 and V-GITM. One standard deviation for V-GITM densities is plotted as a colored area.

3.3 Bulk Neutral Winds and Momentum Sources

The V-GITM winds are self-consistently computed at every time step. They are initialized to zero except the bottom zonal superrotating boundary condition. The objective of solving for the winds explicitly is to better understand how the neutral winds in Venus' thermosphere drive atmospheric processes.

As shown in Figure 10, the mesosphere and lower thermosphere have a retrograde superrotating zonal (RSZ) circulation pattern. At the top of the thermosphere, EUV deposition creates a large pressure gradient that drives the winds poleward on the dayside at mid latitudes and towards the nightside at low latitudes. These circulation patterns create a large altitudinal velocity shear at the morning terminator where the effects of viscosity are large. The vertical shearing makes it difficult to predict the wind pattern in the transition region between the cloud tops (RSZ flow) and the thermosphere/exosphere boundary (subsolar to antisolar flow). Wind measurements taken by the MESSENGER (only sampling up to 110 km) spacecraft show that the westward maximum wind speeds range from 97-143 m/s [*Per-*

611 *alta et al.*, 2017]. In the sampling range, the maximum occurred between 75-90 km. This
612 may suggest a good constraint for the boundary conditions at 70 km. Simulations were per-
613 formed with different lower boundary conditions on the zonal flow to understand the impact
614 this may have.

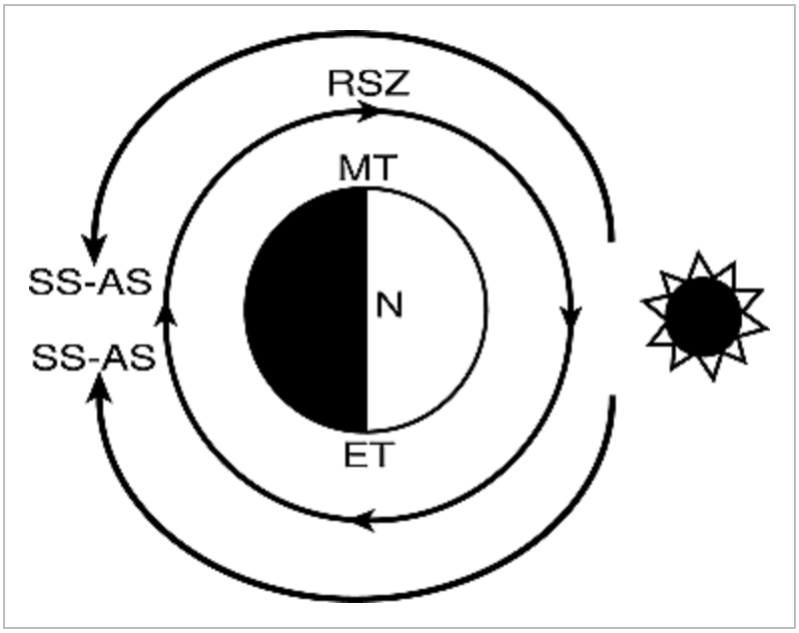

600 **Figure 10.** Depiction of the retrograde super rotating zonal (RSZ) circulation in the lower atmosphere of
601 Venus with the subsolar (SS) to antisolar (AS) flow at higher altitudes. Adapted from [*Schubert et al.*, 2007]

615 Horizontal winds, vertical winds, and temperatures produced by V-GITM are shown in
616 Figures 11 and 12 with different lower boundary condition on the zonal winds of 0 m/s, 50
617 m/s and 100 m/s. Beginning at 90 km, the horizontal velocity almost identically matches the
618 corresponding boundary condition due to the effects of viscosity from the lower layers. The
619 vertical winds are less than 1 m/s.

620 The simulated zonal winds at 105 km are a superposition of the day-to-night flow
621 generated due to the large pressure gradient (from near IR at 105 km), which intensifies as
622 the boundary condition zonal wind is increased. This is most apparent at the terminators,
623 particularly at low latitudes. Meridional winds are orthogonal to the zonal winds and so they
624 do not vary much for a specific zonal boundary condition.

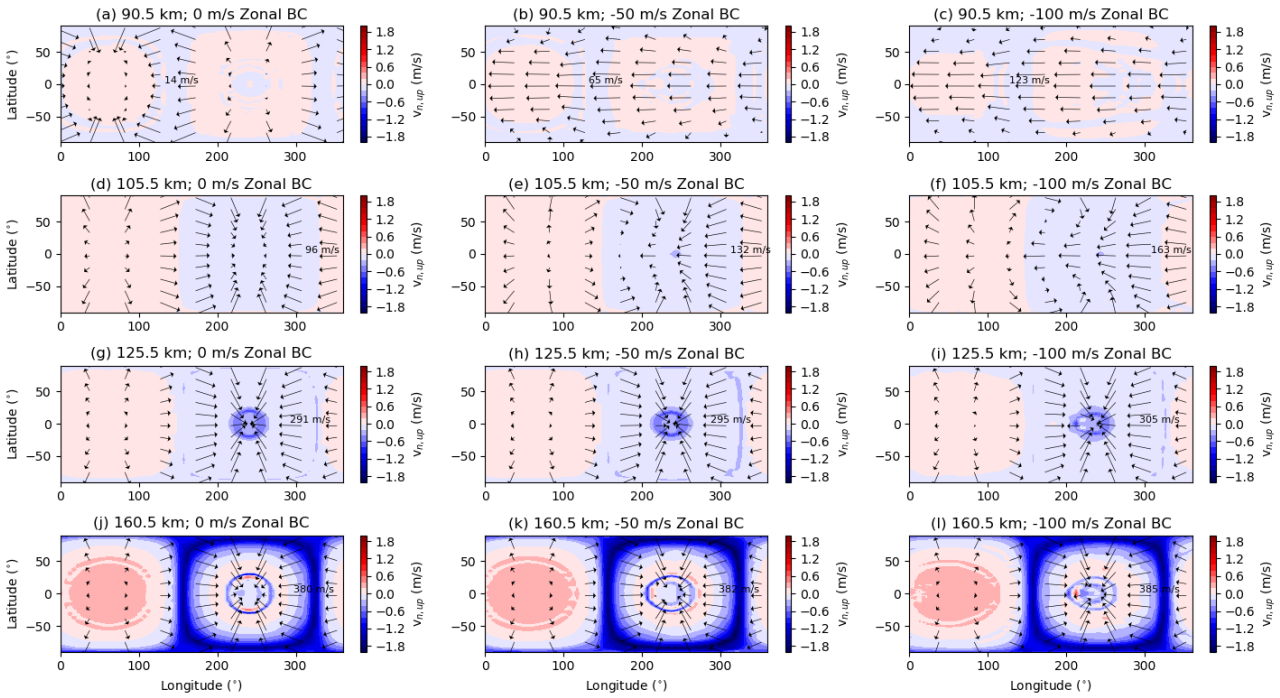

Figure 11. Constant altitude slices of horizontal (arrows) and vertical (contours) winds at 90.5 km (first row), 105.5 km (second row), 125.5 km (third row) and 160.5 km (final row). From left to right, columns show lower boundary conditions of 0 m/s, -50 m/s and -100 m/s. Positive vertical wind values correspond to upward motion. Note that the wind vector length scale changes in each plot, while the vertical wind color scale does not.

At 125 km, velocities are noticeably different than the 105 km horizontal velocities. The 0 m/s boundary condition (see Figure 11g) has a SS-AS pattern which is also driven by the dayside temperature peak, except that the max velocities are much faster. Subplots (g)-(i) do not vary much and the velocities are all within $\pm$20 m/s indicating that influence of RSZ is much less at this altitude and above. The non-zero boundary conditions runs at 160 km behave in a similar fashion despite the low difference in horizontal wind speeds.

Figure 12 shows the nightside, 1°N latitude cross-section of temperature for the 0 m/s, -50 m/s and -100 m/s zonal boundary condition runs. With the 0 m/s run condition, the horizontal winds at high altitudes converge on the nightside producing a small amount of adiabatic heating as described above. The midnight convergence causes the midnight temperatures to be warmest for the -100 m/s RSZ case.

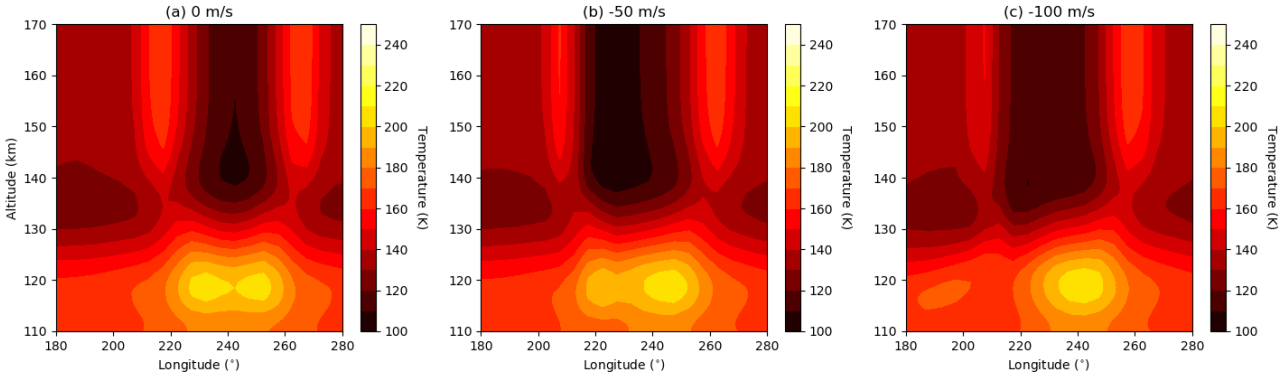

Figure 12. Equator slices of temperatures from 110-170 km on the nightside. From left to right, the lower boundary condition is (a) 0 m/s, (b) -50 m/s or (c) -100 m/s.

Figure 13 shows the zonal accelerations for the -100 m/s run condition at different local times. A description of these momentum sources, although described in the vertical direction, are discussed in equations 2 and 3. For the specific horizontal momentum equation, please refer to [*Ridley et al.*, 2006]. As previously mentioned, the near IR and solar EUV create warm regions on the dayside. The solar flux is deposited over a large area so the pressure gradient term at noon is not particularly large. The largest temperature and pressure gradients occur at the terminators and are much stronger than any other acceleration term at these locations. Although included in the momentum equation, ion drag is a negligible forcing on the neutrals since there are no magnetic and electric fields to drive the ion motion. For this reason, after a short amount of time the neutrals drag on the ions which accelerates them to move in unison with one another leading to no expected ion drag. However, ion winds from the solar wind interaction may drag neutrals at higher altitudes [*Brecht and Ledvina*, 2021].

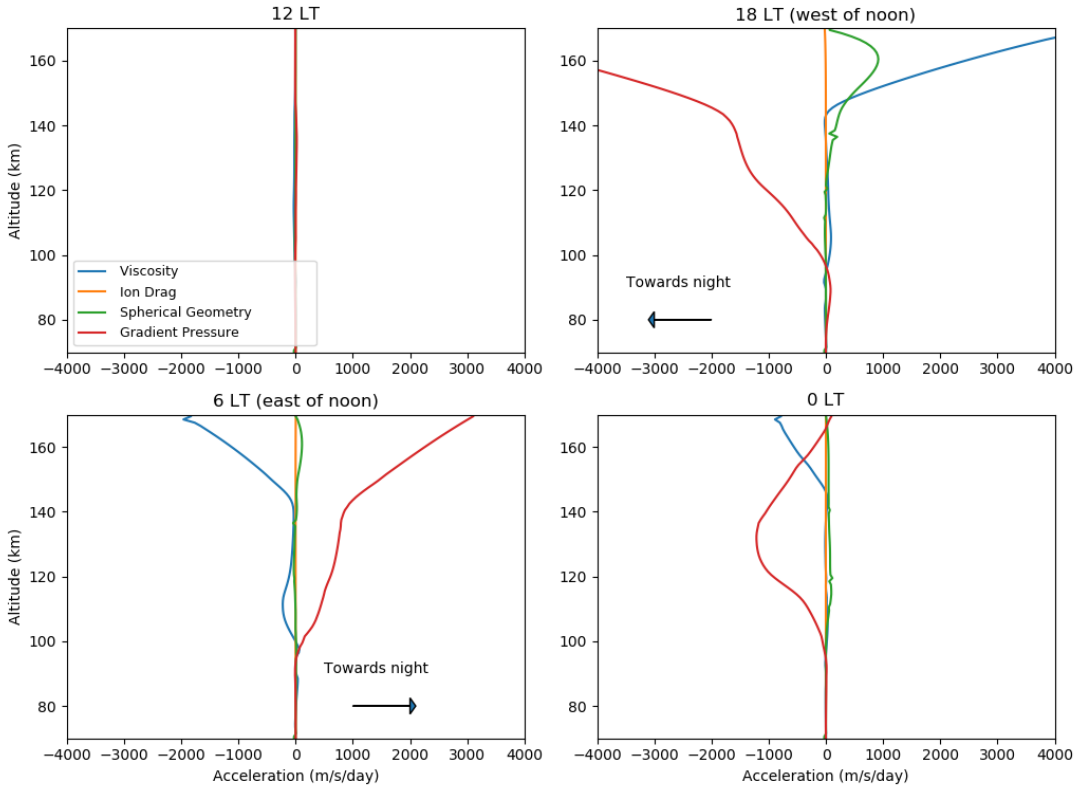

Figure 13. Momentum sources at equator in the zonal (east/west) direction for the -100 m/s base case at four different local times.

3.4 Shock-like Features within V-GITM

A higher resolution simulation was performed matching the horizontal resolution in *Navarro et al.* [2021]. The standard resolution used up to this point and the Navarro resolution runs are compared in Figure 14. Following some of the metrics in their work, V-GITM showed supersonic winds on the nightside and a "hot ring" around midnight during two simulations with different horizontal resolutions. Mach numbers reach a value of 2 east of midnight. West of midnight, the mach number is also supersonic with a lower value of 1.6. The lower resolution was performed at $5^\circ \times 2^\circ$ while the *Navarro et al.* [2021] is performed at $3.75^\circ \times 1.875^\circ$. Over a distance of roughly 500 km, the flow is slowed to subsonic speeds in both simulations. In addition to the supersonic speeds, the η indicator pointed out in [*Navarro et al.*, 2021] [*Zhu et al.*, 2013] [*Fromang, Sébastien et al.*, 2016] provides a dimensionless quantity to assess the presence of a shock where the η is greater than 0.2. Equatorial values of η were computed at 130 km and 160 km, η remained below 0.2 across

all longitudes except around 200-210° and around 250-255°. These longitudes are consistent with the crossings of supersonic to subsonic flows in Figure 14c and 14d. As mentioned in *Navarro et al.* [2021], an enhanced model is needed to accurately handle shock formation because fluid models, even if non-hydrostatic, do not resolve supersonic shock effects.

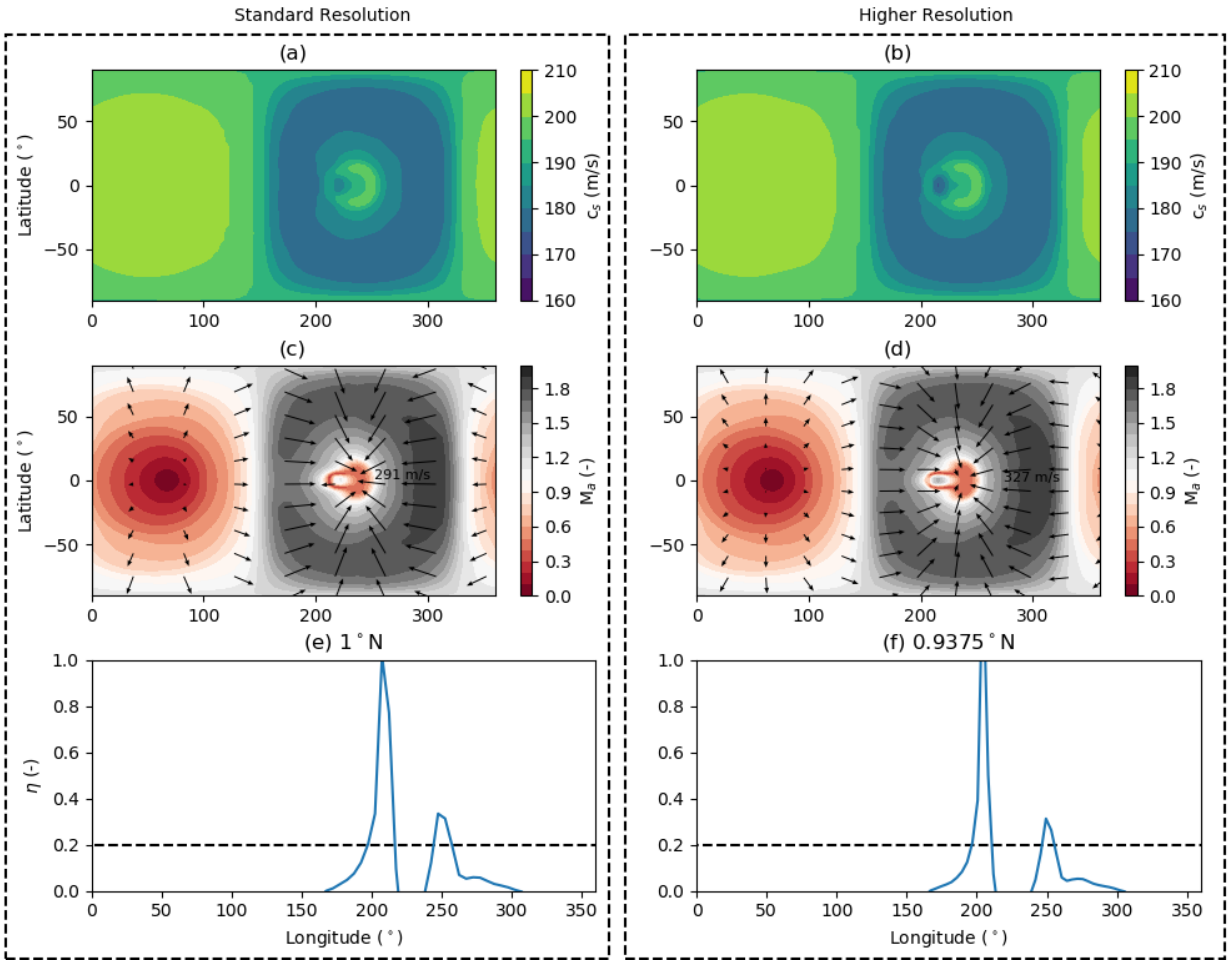

Figure 14. The speed of sound (c_s) and Mach number (M_a) and a dimensionless quantity (η) are shown at 130.5 km for two different horizontal resolutions. In (e) and (f), η describes flow divergence was computed at all longitudes near the equator. A black, dashed line showing a threshold of 0.2 is plotted to help distinguish shock locations.

3.5 Ionosphere

V-GITM's ionosphere is driven by the photochemistry described in Table 3 and coupled ion-neutral dynamics described above. In this section, individual ion density profiles

and bulk electron densities are shown in Figure 15. The dayside ionosphere is robust, with densities peaking at over 10^5 cm^{-3} which is consistent with Venus Express measurements taken during solar minimum [*Hensley et al.*, 2020]. Near midnight, however, a more meager ionosphere exists with the main density being NO^+ which peak values are greater than 10^1 cm^{-3} at 170 km. On the nightside nearer either terminator, the electron density has a peak of 10^3 cm^{-3}. The ion population at these locations consist of a relatively equal amount of NO^+ and O_2^+. O_2^+ is advected to the nightside, but not fully across the anti-solar point which explains the lack of O_2^+ at midnight in Figure 15.

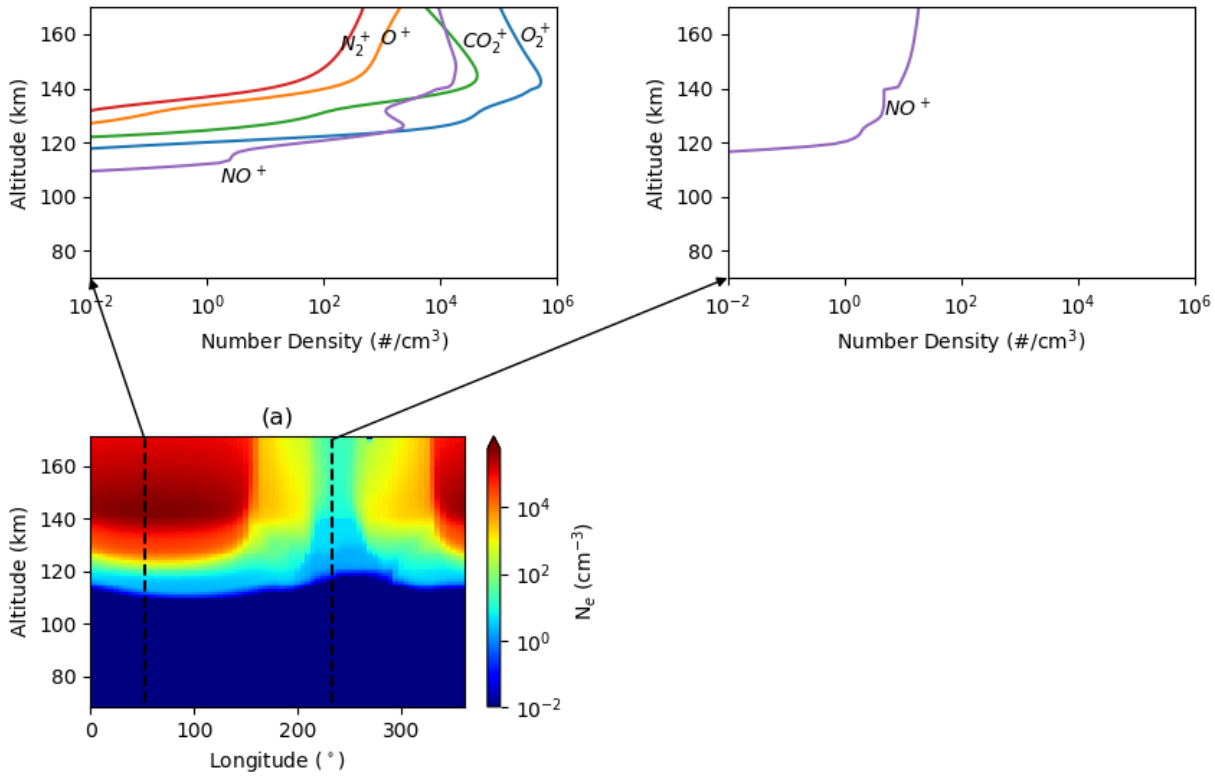

Figure 15. Electron densities at the equator with altitude slices showing species-specific ion densities at noon (left) and midnight (right).

Figure 16 provides a side-by-side comparison of the neutral and ion velocities at 140.5 km. This location was selected due to O_2^+ being the only species advected and 140 km is near the dayside density peak. The ions and neutrals have been shown to move in unison in the zonal and meridional directions. As seen in Figure 16b, the ion vertical velocities have a

large downflow on the nightside not seen in the neutrals. This location corresponds to a density of O_2^+ less than 10^2 cm^{-3} and is believed to not be physical nor a significant detraction from the other findings of this simulation.

The midnight cross-section of the ion population (see Figure 15) shows only NO^+ despite not being an advected ion. Given the neutral profiles shown in section 3.2, the primary reactions creating NO^+ are R15 and R18. NO^+ is lost through electron recombination. Balancing the mass flow rate reaction rates showed that NO^+ will stay roughly 50x larger than the corresponding O_2^+ density. This relationship will hold until additional the NO^+ reaction rate coefficient is re-examined or additional NO^+ loss terms are added.

Overall, the nighttime electron densities are between two to four orders of magnitude less than the simulated dayside. *Taylor Jr. et al.* [1980] has indicated the day-night difference should be one to three orders of magnitude smaller with the same composition. *Cravens et al.* [1982] concluded that the nightside ionosphere is highly variable. Occasionally it would be completely depleted ($[e^-] < 10^2$ cm^{-3}), most of the time it showed irregularities and sometimes it was smooth with maximums between 10^4 and 10^5 cm^{-3}.

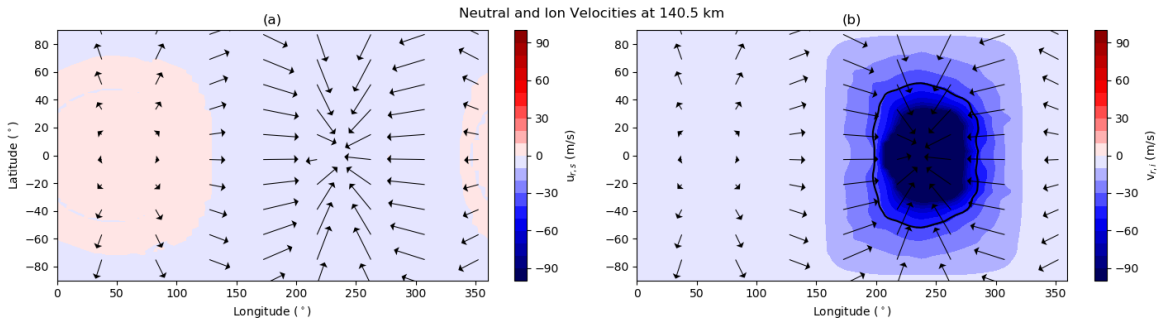

Figure 16. Ion and neutral velocities at 140.5 km. Horizontal velocities for the (a) neutrals and (b) ions are plotted as arrows with the corresponding vertical velocity plotted as a contour in the background. A contour line of $n_{O_2^+}$ = 10^2 cm^{-3} is plotted in (b).

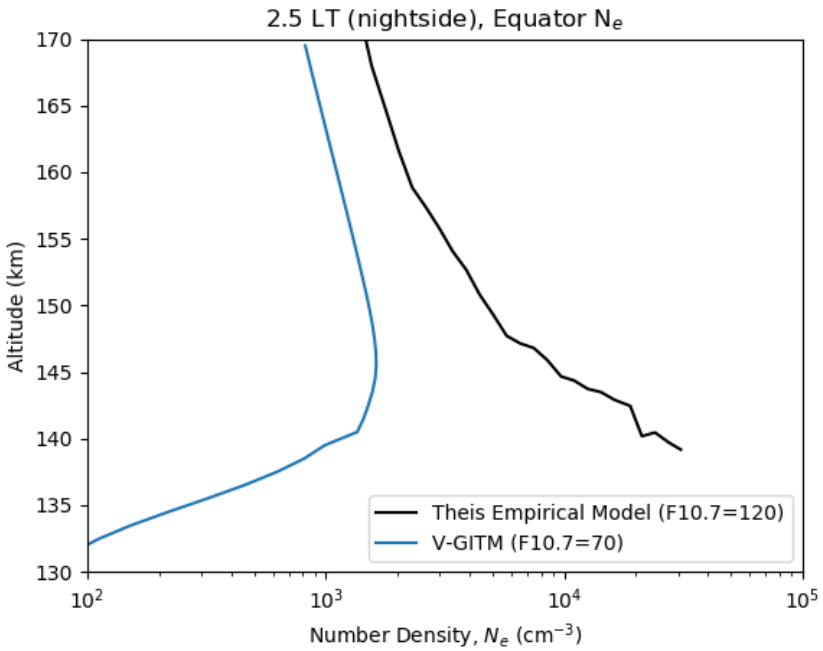

Figure 17. Electron density structure at the equator for 2.5 LT for the empirical model from [*Theis and Brace*, 1993] and V-GITM.

Figure 17 shows a data-model comparison of the nightside electron density at 2.5 LT from *Theis and Brace* [1993] (in black) and V-GITM results (in blue). It is not expected to have the same electron densities between the lines due to the inherent difference in solar activity. *Theis and Brace* [1993] has shown that between F10.7 values of 120 $Wm^{-2}Hz^{-1}$ and 200 $Wm^{-2}Hz^{-1}$ that the electron density peak does not vary much near 140 km. *Knudsen* [1987] points out that dayside electron densities may have an effects on the day-to-night flow of plasma.

Spenner et al. [1981] and *Kliore et al.* [1991] also indicate that transport of O^+ from the dayside is a source of night-time ionosphere, but V-GITM does not extend at high enough altitudes to properly attempt to capture this effect. The influence of a nightside upper boundary condition for O^+ will be explored in future work to simulate this effect. Precipitation of solar wind light ions or electrons onto the nightside is the other mechanism that is often considered [*Gringauz et al.*, 1979]. The lack of this process in the physics for V-GITM may explain why the observed peak is not matching, but is beyond the scope of this paper.

4 Summary and Conclusion

This paper introduces the main features of a new Venus global circulation model of the ionosphere-thermosphere region. The new model, V-GITM, is based on the terrestrial GITM model [*Ridley et al.*, 2006] and Mars counterpart [*Bougher et al.*, 2015]. V-GITM utilizes Venus specific parameters and physical processes from several existing Venus codes, including the Venus Thermosphere General Circulation Model (VTGCM) and LMD-IPSL's V-PCM. V-GITM self-consistently solves for the neutral densities, winds, and temperatures as well as the ion and electron densities, and the ion velocities while assuming a partially dynamical ionosphere. Overall, this is the first Venus model to couple the ionosphere-thermosphere without assuming hydrostatic equilibrium and uses chemical heating to correctly approximate energy depositing from the solar EUV.

Comparisons between the model results and a wide range of neutral and ion measurements across a variety of local times are shown. Dayside neutral temperature and bulk density structure of the upper atmosphere match reasonably well, although species-specific densities do not always match other models' predictions. Neutral winds are shown including a variety of retrograde superrotating zonal flow speeds demonstrating the strong influence on neutral wind profiles up to 100 km, but having a relatively minor impact on wind speeds in the upper thermosphere and dayside temperatures. Finally, V-GITM explored the ion velocities and nighttime ionosphere that forms from only the advection of O_2^+.

Introducing V-GITM, with all of its features, allows the Venus modeling community to perform more insightful model-model comparisons to determine the importance of a hydrostatic solver, ion dynamics and exothermic heating. Further work is needed for all Venus models to improve upon inaccurate approximations or parameterizations of the physics implemented. Processes like eddy diffusion, 15 μm CO_2 cooling and solar IR heating are complicated to correctly model alone are thus parameterized, which makes them highly uncertain. It is understood that each of these significantly affect Venus' thermosphere and so future studies about quantifying the uncertainty of these terms is an important topic so that this model can be a useful tool for future Venus studies, particularly with the upcoming VERITAS and DAVINCI missions scheduled.

5 Open Research

V-GITM is freely available through GitHub [*Ridley et al.*, 2023]. Plotting routines and data within this work will be published on DeepBlue.

Acknowledgements

The research presented in this study was supported at University of Michigan partially by the joint NSF-NASA Space Weather with Quantified Uncertainties program under NSF grant number 2028125 and NASA grant number 80NSSC20K1581. This work was also supported by the NASA grant 80NSSC19K0562. This research has made use of the NASA Exoplanet Archive, which is operated by the California Institute of Technology, under contract with the National Aeronautics and Space Administration under the Exoplanet Exploration Program.

References

Bannister, R. N. (2001), A guide to computing orbital positions of major solar system bodies: forward and inverse calculations, *Data Assimilation Research Center, University of Reading, U.K*, pp. 19–23.

Barnes, R. (2017), Tidal locking of habitable exoplanets, *Celest Mech Dyn Astr*, *129*, 509–536, doi:10.1007/s10569-017-9783-7.

Bertaux, J.-L., D. Nevejans, O. Korablev, E. Villard, E. Quémerais, E. Neefs, F. Montmessin, F. Leblanc, J. Dubois, E. Dimarellis, A. Hauchecorne, F. Lefèvre, P. Rannou, J. Chaufray, M. Cabane, G. Cernogora, G. Souchon, F. Semelin, A. Reberac, E. Van Ransbeek, S. Berkenbosch, R. Clairquin, C. Muller, F. Forget, F. Hourdin, O. Talagrand, A. Rodin, A. Fedorova, A. Stepanov, I. Vinogradov, A. Kiselev, Y. Kalinnikov, G. Durry, B. Sandel, A. Stern, and J. Gérard (2007), Spicav on venus express: Three spectrometers to study the global structure and composition of the venus atmosphere, *Planetary and Space Science*, *55*(12), 1673–1700, doi:https://doi.org/10.1016/j.pss.2007.01.016, the Planet Venus and the Venus Express Mission, Part 2.

Bougher, S., R. Dickinson, E. Ridley, and R. Roble (1988), Venus mesosphere and thermosphere: Iii. three-dimensional general circulation with coupled dynamics and composition, *Icarus*, *73*(3), 545 – 573, doi:https://doi.org/10.1016/0019-1035(88)90064-4.

Bougher, S. W., D. M. Hunten, and R. G. Roble (1994), Co2 cooling in terrestrial planet thermospheres, *Journal of Geophysical Research: Planets*, *99*(E7), 14,609–14,622, doi:https://doi.org/10.1029/94JE01088.

Bougher, S. W., S. Engel, R. G. Roble, and B. Foster (1999), Comparative terrestrial planet thermospheres: 2. solar cycle variation of global structure and winds at equinox, *Journal of Geophysical Research: Planets*, *104*(E7), 16,591–16,611, doi:https://doi.org/10.1029/1998JE001019.

Bougher, S. W., P.-L. Blelly, M. Combi, J. L. Fox, I. Mueller-Wodarg, A. J. Ridley, and R. G. Roble (2008), Neutral upper atmosphere and ionosphere modeling, *Space Sci Rev*, *139*(63), 107–141, doi:10.1007/s11214-008-9401-9.

Bougher, S. W., D. Pawlowski, J. M. Bell, S. Nelli, T. McDunn, J. R. Murphy, M. Chizek, and A. Ridley (2015), Mars global ionosphere-thermosphere model: Solar cycle, seasonal, and diurnal variations of the mars upper atmosphere, *Journal of Geophysical Research: Planets*, *120*(2), 311–342, doi:10.1002/2014JE004715.

Bougher, S. W., K. J. Roeten, K. Olsen, P. R. Mahaffy, M. Benna, M. Elrod, S. K. Jain, N. M. Schneider, J. Deighan, E. Thiemann, F. G. Eparvier, A. Stiepen, and B. M. Jakosky (2017), The structure and variability of mars dayside thermosphere from maven ngims and iuvs measurements: Seasonal and solar activity trends in scale heights and temperatures, *Journal of Geophysical Research: Space Physics*, *122*(1), 1296–1313, doi: https://doi.org/10.1002/2016JA023454.

Bougher, S. W., M. Benna, M. Elrod, K. Roeten, and E. Thiemann (2023), Maven/ngims dayside exospheric temperatures over solar cycle and seasons: Role of dayside thermal balances in regulating temperatures, *Journal of Geophysical Research: Planets*, *128*(1), e2022JE007,475, doi:https://doi.org/10.1029/2022JE007475, e2022JE007475 2022JE007475.

Brecht, A., S. Bougher, J.-C. Gérard, and L. Soret (2012), Atomic oxygen distributions in the venus thermosphere: Comparisons between venus express observations and global model simulations, *Icarus*, *217*(2), 759–766, doi:https://doi.org/10.1016/j.icarus.2011.06.033, advances in Venus Science.

Brecht, A. S., S. W. Bougher, J. C. Gérard, C. D. Parkinson, S. Rafkin, and B. Foster (2011), Understanding the variability of nightside temperatures, no uv and o2 ir nightglow emissions in the venus upper atmosphere, *Journal of Geophysical Research: Planets*, *116*(E8), doi:https://doi.org/10.1029/2010JE003770.

Brecht, S. H., and S. A. Ledvina (2021), An explanation of the nightside ionospheric structure of venus, *Journal of Geophysical Research: Space Physics*, *126*(2), e2020JA027,779, doi:https://doi.org/10.1029/2020JA027779, e2020JA027779 2020JA027779.

Chamberlin, P. C., T. N. Woods, and F. G. Eparvier (2008), Flare irradiance spectral model (fism): Flare component algorithms and results, *Space Weather*, *6*(5), doi: 10.1029/2007SW000372.

Colegrove, F. D., F. S. Johnson, and W. B. Hanson (1966), Atmospheric composition in the lower thermosphere, *Journal of Geophysical Research (1896-1977)*, *71*(9), 2227–2236, doi:https://doi.org/10.1029/JZ071i009p02227.

Cravens, T., L. Brace, H. Taylor, C. Russell, W. Knudsen, K. Miller, A. Barnes, J. Mihalov, F. Scarf, S. Quenon, and A. Nagy (1982), Disappearing ionospheres on the nightside of venus, *Icarus*, *51*(2), 271–282, doi:https://doi.org/10.1016/0019-1035(82)90083-5.

Crisp, D. (1986), Radiative forcing of the venus mesosphere: I. solar fluxes and heating rates, *Icarus*, *67*(3), 484–514, doi:https://doi.org/10.1016/0019-1035(86)90126-0.

Dickinson, R. E., E. C. Ridley, and R. G. Roble (1984), Thermospheric general circulation with coupled dynamics and composition., *Journal of Atmospheric Sciences*, *41*, 205–219, doi:10.1175/1520-0469(1984)041⟨0205:TGCWCD⟩2.0.CO;2.

Ehrenreich, D., and Désert, J.-M. (2011), Mass-loss rates for transiting exoplanets, *A&A*, *529*, A136, doi:10.1051/0004-6361/201016356.

Eparvier, F. G., P. C. Chamberlin, T. N. Woods, and E. M. B. Thiemann (2015), The solar extreme ultraviolet monitor for maven, *Space Science Reviews*, *195*(1-4), 293–301, doi:10.1007/s11214-015-0195-2.

Fox, J. L. (1985), The O_2^+ vibrational distribution in the Venusian ionosphere, *Advances in Space Research*, *5*(9), 165–169, doi:10.1016/0273-1177(85)90285-6.

Fox, J. L., and K. Y. Sung (2001), Solar activity variations of the venus thermosphere/ionosphere, *Journal of Geophysical Research: Space Physics*, *106*(A10), 21,305–21,335, doi:https://doi.org/10.1029/2001JA000069.

Fromang, Sébastien, Leconte, Jeremy, and Heng, Kevin (2016), Shear-driven instabilities and shocks in the atmospheres of hot jupiters, *A&A*, *591*, A144, doi:10.1051/0004-6361/201527600.

Garvin, J. B., S. A. Getty, G. N. Arney, N. M. Johnson, E. Kohler, K. O. Schwer, M. Sekerak, A. Bartels, R. S. Saylor, V. E. Elliott, C. S. Goodloe, M. B. Garrison, V. Cottini, N. Izenberg, R. Lorenz, C. A. Malespin, M. Ravine, C. R. Webster, D. H. Atkinson, S. Aslam, S. Atreya, B. J. Bos, W. B. Brinckerhoff, B. Campbell, D. Crisp, J. R. Filiberto, F. Forget, M. Gilmore, N. Gorius, D. Grinspoon, A. E. Hofmann, S. R. Kane, W. Kiefer, S. Lebonnois, P. R. Mahaffy, A. Pavlov, M. Trainer, K. J. Zahnle, and M. Zolotov (2022), Revealing the mysteries of venus: The DAVINCI mission, *The Planetary Science Journal*, *3*(5), 117, doi:10.3847/psj/ac63c2.

Gilli, G., M. López-Valverde, J. Peralta, S. Bougher, A. Brecht, P. Drossart, and G. Piccioni (2015), Carbon monoxide and temperature in the upper atmosphere of venus from virtis/venus express non-lte limb measurements, *Icarus*, *248*, 478–498, doi:https://doi.org/10.1016/j.icarus.2014.10.047.

Gilli, G., S. Lebonnois, F. González-Galindo, M. López-Valverde, A. Stolzenbach, F. Lefèvre, J. Chaufray, and F. Lott (2017), Thermal structure of the upper atmosphere of venus simulated by a ground-to-thermosphere gcm, *Icarus*, *281*, 55–72, doi:https://doi.org/10.1016/j.icarus.2016.09.016.

Gilli, G., T. Navarro, S. Lebonnois, D. Quirino, V. Silva, A. Stolzenbach, F. Lefèvre, and G. Schubert (2021), Venus upper atmosphere revealed by a gcm: Ii. model validation with temperature and density measurements, *Icarus*, *366*, 114,432, doi: https://doi.org/10.1016/j.icarus.2021.114432.

González-Galindo, F., J.-Y. Chaufray, M. A. López-Valverde, G. Gilli, F. Forget, F. Leblanc, R. Modolo, S. Hess, and M. Yagi (2013), Three-dimensional martian ionosphere model: I. the photochemical ionosphere below 180 km, *Journal of Geophysical Research: Planets*, *118*(10), 2105–2123, doi:https://doi.org/10.1002/jgre.20150.

Gringauz, K. I., M. I. Verigin, T. K. Breus, and T. Gombosi (1979), The interaction of electrons in the optical umbra of venus with the planetary atmosphere—the origin of the nighttime ionosphere, *Journal of Geophysical Research: Space Physics*, *84*(A5), 2123–2127, doi:https://doi.org/10.1029/JA084iA05p02123.

Gu, H., J. Cui, D.-D. Niu, Y.-T. Cao, X.-S. Wu, J. Li, Z.-P. Wu, F. He, and Y. Wei (2020), Neutral heating efficiency in the dayside martian upper atmosphere, *The Astronomical Journal*, *159*(2), 39, doi:10.3847/1538-3881/ab5fcc.

Heays, A. N., Bosman, A. D., and van Dishoeck, E. F. (2017), Photodissociation and photoionisation of atoms and molecules of astrophysical interest, *A&A*, *602*, A105, doi: 10.1051/0004-6361/201628742.

Hedin, A. E., H. B. Niemann, W. T. Kasprzak, and A. Seiff (1983), Global empirical model of the venus thermosphere, *Journal of Geophysical Research: Space Physics*, *88*(A1), 73–83, doi:10.1029/JA088iA01p00073.

Hensley, K., P. Withers, Z. Girazian, M. Pätzold, S. Tellmann, and B. Häusler (2020), Dependence of dayside electron densities at venus on solar irradiance, *Journal of Geophysical Research: Space Physics*, *125*(2), e2019JA027,167, doi:https://doi.org/10.1029/2019JA027167, e2019JA027167 10.1029/2019JA027167.

Hoshino, N., H. Fujiwara, M. Takagi, Y. Takahashi, and Y. Kasaba (2012), Characteristics of planetary-scale waves simulated by a new venusian mesosphere and thermosphere general circulation model, *Icarus*, *217*(2), 818–830, doi:https://doi.org/10.1016/j.icarus.2011.06.039, advances in Venus Science.

Hoshino, N., H. Fujiwara, M. Takagi, and Y. Kasaba (2013), Effects of gravity waves on the day-night difference of the general circulation in the venusian lower thermosphere, *Journal of Geophysical Research: Planets*, *118*(10), 2004–2015, doi: https://doi.org/10.1002/jgre.20154.

Huestis, D. L., S. W. Bougher, J. L. Fox, M. Galand, R. E. Johnson, M. J. I., and J. C. Pickering (2008), Cross sections and reaction rates for comparative planetary aeronomy, *Space Sci Rev*, *139*(63), doi:https://doi.org/10.1007/s11214-008-9383-7.

Häusler, B., M. Pätzold, G. Tyler, R. Simpson, M. Bird, V. Dehant, J.-P. Barriot, W. Eidel, R. Mattei, S. Remus, J. Selle, S. Tellmann, and T. Imamura (2006), Radio science investigations by vera onboard the venus express spacecraft, *Planetary and Space Science*, *54*(13), 1315–1335, doi:https://doi.org/10.1016/j.pss.2006.04.032, the Planet Venus and the Venus Express Mission.

Jain, S. K., S. W. Bougher, J. Deighan, N. M. Schneider, F. González Galindo, A. I. F. Stewart, R. Sharrar, D. Kass, J. Murphy, and D. Pawlowski (2020), Martian thermospheric warming associated with the planet encircling dust event of 2018, *Geophysical Research Letters*, *47*(3), e2019GL085,302, doi:https://doi.org/10.1029/2019GL085302, e2019GL085302 10.1029/2019GL085302.

Keating, G., J. Bertaux, S. Bougher, R. Dickinson, T. Cravens, A. Nagy, A. Hedin, V. Krasnopolsky, J. Nicholson, L. Paxton, and U. von Zahn (1985), Models of venus neutral upper atmosphere: Structure and composition, *Advances in Space Research*, *5*(11), 117–171, doi:https://doi.org/10.1016/0273-1177(85)90200-5.

Keating, G. M., R. H. Tolson, and E. W. Hinson (1979), Venus thermosphere and exosphere: First satellite drag measurements of an extraterrestrial atmosphere, *Science*, *203*(4382), 772–774, doi:10.1126/science.203.4382.772.

Kliore, A., V. Moroz, and G. Keating (1985), *The Venus International Reference Atmosphere.*, vol. 5.

Kliore, A. J., I. R. Patel, A. F. Nagy, T. E. Cravens, and T. I. Gombosi (1979), Initial observations of the nightside ionosphere of venus from pioneer venus orbiter radio occultations, *Science*, *205*(4401), 99–102, doi:10.1126/science.205.4401.99.

Kliore, A. J., J. G. Luhmann, and M. H. G. Zhang (1991), The effect of the solar cycle on the maintenance of the nightside ionosphere of venus, *Journal of Geophysical Research: Space Physics*, *96*(A7), 11,065–11,071, doi:https://doi.org/10.1029/91JA00672.

Knudsen, W. C. (1987), Frequency functions of venus nightside ion densities, *Journal of Geophysical Research: Space Physics*, *92*(A7), 7308–7316, doi:https://doi.org/10.1029/JA092iA07p07308.

Knudsen, W. C. (1992), *The Venus Ionosphere from in Situ Measurements*, pp. 237–263, American Geophysical Union (AGU), doi:https://doi.org/10.1029/GM066p0237.

Korablev, O., J. L. Bertaux, D. Nevejans, and S. I. Team (2003), Compact High-Resolution IR Spectrometer for Atmospheric Studies, *EAEJA*, p. 14785.

Krehbiel, J. P., L. H. Brace, R. F. Theis, J. R. Cutler, W. H. Pinkus, and R. B. Kaplan (1980), Pioneer venus orbiter electron temperature probe, *IEEE Transactions on Geoscience and Remote Sensing*, *GE-18*(1), 49–54, doi:10.1109/TGRS.1980.350260.

Limaye, S. S., S. Lebonnois, A. Mahieux, M. Pätzold, S. Bougher, S. Bruinsma, S. Chamberlain, R. T. Clancy, J.-C. Gérard, G. Gilli, D. Grassi, R. Haus, M. Herrmann, T. Imamura, E. Kohler, P. Krause, A. Migliorini, F. Montmessin, C. Pere, M. Persson, A. Piccialli, M. Rengel, A. Rodin, B. Sandor, M. Sornig, H. Svedhem, S. Tellmann, P. Tanga, A. C. Vandaele, T. Widemann, C. F. Wilson, I. Müller-Wodarg, and L. Zasova (2017), The thermal structure of the venus atmosphere: Intercomparison of venus express and ground based observations of vertical temperature and density profiles, *Icarus*, *294*, 124–155, doi:https://doi.org/10.1016/j.icarus.2017.04.020.

López-Valverde, M. A., D. P. Edwards, M. López-Puertas, and C. Roldán (1998), Non-local thermodynamic equilibrium in general circulation models of the martian atmosphere 1. effects of the local thermodynamic equilibrium approximation on thermal cooling and solar heating, *Journal of Geophysical Research: Planets*, *103*(E7), 16,799–16,811, doi:https://doi.org/10.1029/98JE01601.

Machado, P., D. Luz, T. Widemann, E. Lellouch, and O. Witasse (2012), Mapping zonal winds at venus's cloud tops from ground-based doppler velocimetry, *Icarus*, *221*(1), 248–261, doi:https://doi.org/10.1016/j.icarus.2012.07.012.

Machado, P., T. Widemann, J. Peralta, R. Gonçalves, J.-F. Donati, and D. Luz (2017), Venus cloud-tracked and doppler velocimetry winds from cfht/espadons and venus express/virtis in april 2014, *Icarus*, *285*, 8–26, doi:https://doi.org/10.1016/j.icarus.2016.12.017.

Mahieux, A., S. Berkenbosch, R. Clairquin, D. Fussen, N. Mateshvili, E. Neefs, D. Nevejans, B. Ristic, A. C. Vandaele, V. Wilquet, D. Belyaev, A. Fedorova, O. Korablev, E. Villard, F. Montmessin, and J.-L. Bertaux (2008), In-flight performance and calibration of spicav soir onboard venus express, *Applied Optics*, *47*(13), 2252 – 2265, doi:10.1364/AO.47.002252, cited by: 48.

Mahieux, A., R. Yelle, N. Yoshida, S. Robert, A. Piccialli, H. Nakagawa, Y. Kasaba, F. Mills, and A. Vandaele (2021), Determination of the venus eddy diffusion profile from co and co2 profiles using soir/venus express observations, *Icarus*, *361*, 114,388, doi:https://doi.org/10.1016/j.icarus.2021.114388.

Malhotra, G., and A. Ridley (2020), Impacts of Spatially Varying Eddy Diffusion Coefficient in the Lower Thermosphere on the Ionosphere and Thermosphere using GITM, in *AGU Fall Meeting Abstracts*, vol. 2020, pp. SA001–0014.

Martinez, A., A. S. Brecht, H. Karyu, S. Lebonnois, S. W. Bougher, T. Kuroda, Y. Kasaba, G. Gilli, T. Navarro, and H. Sagawa (2021), Venusian Upper Mesosphere and Lower Thermosphere GCMs Intercomparison Project, in *LPI Contributions*, *LPI Contributions*, vol. 2628, p. 8045.

Martinez, A., S. Lebonnois, E. Millour, T. Pierron, E. Moisan, G. Gilli, and F. Lefèvre (2023), Exploring the variability of the venusian thermosphere with the ipsl venus gcm, *Icarus*, *389*, 115,272, doi:https://doi.org/10.1016/j.icarus.2022.115272.

Moroz, V., and L. Zasova (1997), Vira-2: A review of inputs for updating the venus international reference atmosphere, *Advances in Space Research*, *19*(8), 1191–1201, doi:https://doi.org/10.1016/S0273-1177(97)00270-6, planetary Atmospheres and Ionospheres and Reference Atmospheres.

Navarro, T., G. Gilli, G. Schubert, S. Lebonnois, F. Lefèvre, and D. Quirino (2021), Venus' upper atmosphere revealed by a gcm: I. structure and variability of the circulation, *Icarus*, *366*, 114,400, doi:https://doi.org/10.1016/j.icarus.2021.114400.

Parkinson, C., S. Bougher, F. Mills, Y. Yung, A. Brecht, D. Shields, and M. Liemohn (2021), Modeling of observations of the oh nightglow in the venusian mesosphere, *Icarus*, *368*, 114,580, doi:https://doi.org/10.1016/j.icarus.2021.114580.

Peralta, J., Y. J. Lee, R. Hueso, R. T. Clancy, B. J. Sandor, A. Sánchez-Lavega, E. Lellouch, M. Rengel, P. Machado, M. Omino, A. Piccialli, T. Imamura, T. Horinouchi, S. Murakami, K. Ogohara, D. Luz, and D. Peach (2017), Venus's winds and temperatures during the messenger's flyby: An approximation to a three-dimensional instantaneous state of the atmosphere, *Geophysical Research Letters*, *44*(8), 3907–3915, doi:10.1002/2017GL072900.

Petrignani, A., W. J. van der Zande, P. C. Cosby, F. Hellberg, R. D. Thomas, and M. Larsson (2005), Vibrationally resolved rate coefficients and branching fractions in the dissociative recombination of O2+, *Journal of Chemical Physics*, *122*(1), 014,302–014,302, doi:10.1063/1.1825991.

Rengel, M., P. Hartogh, and C. Jarchow (2008), Hhsmt observations of the venusian mesospheric temperature, winds, and co abundance around the messenger flyby, *Planetary and Space Science*, *56*(13), 1688–1695, doi:https://doi.org/10.1016/j.pss.2008.07.014, advances in Planetary Sciences: AOGS 2007.

Richards, P. G., J. A. Fennelly, and D. G. Torr (1994), Euvac: A solar euv flux model for aeronomic calculations, *Journal of Geophysical Research: Space Physics*, *99*(A5), 8981–8992, doi:https://doi.org/10.1029/94JA00518.

Ridley, A., spacecataz, X. Meng, D. C. S. Öztürk, B. Ponder, and M. Burleigh (2023), Gitm-code/gitm: v23.01.06, doi:https://doi.org/10.5281/zenodo.7509934.

Ridley, A. J., Y. Deng, and G. Tóth (2006), The global ionosphere-thermosphere model, *Journal of Atmospheric and Solar-Terrestrial Physics*, *68*, 839–864.

Roeten, K. J., S. W. Bougher, M. Benna, P. R. Mahaffy, Y. Lee, D. Pawlowski, F. González-Galindo, and M. López-Valverde (2019), Maven/ngims thermospheric neutral wind observations: Interpretation using the m-gitm general circulation model, *Journal of Geophysical Research: Planets*, *124*(12), 3283–3303, doi:https://doi.org/10.1029/2019JE005957.

Roldán, C., M. López-Valverde, M. López-Puertas, and D. Edwards (2000), Non-lte infrared emissions of co2 in the atmosphere of venus, *Icarus*, *147*(1), 11–25, doi:https://doi.org/10.1006/icar.2000.6432.

Rosati, R. E., R. Johnsen, and M. F. Golde (2003), Absolute yields of CO(a$'\ ^3\Sigma^+$, d $^3\Delta_i$,e $^3\Sigma^-$)+O from the dissociative recombination of $CO_2{}^+$ ions with electrons, *J. Comput. Phys.*, *119*(22), 11,630–11,635, doi:10.1063/1.1623480.

Schubert, G., C. Covey, A. D. Genio, L. S. Elson, G. Keating, A. Seiff, R. E. Young, J. Apt, C. C. Counselman III, A. J. Kliore, S. S. Limaye, H. E. Revercomb, L. A. Sromovsky, V. E. Suomi, F. Taylor, R. Woo, and U. von Zahn (1980), Structure and circulation of the venus atmosphere, *Journal of Geophysical Research: Space Physics*, *85*(A13), 8007–8025, doi:https://doi.org/10.1029/JA085iA13p08007.

Schubert, G., S. W. Bougher, C. C. Covey, A. D. Del Genio, A. S. Grossman, J. L. Hollingsworth, S. S. Limaye, and R. E. Young (2007), *Venus Atmosphere Dynamics: A Continuing Enigma*, pp. 101–120, American Geophysical Union (AGU), doi:10.1029/176GM07.

Schunk, R. W., and A. F. Nagy (2004), *Ionospheres*, 570 pp., Cambridge University Press.

Smith III, F. L., and C. Smith (1972), Numerical evaluation of chapman's grazing incidence integral ch (x,), *Journal of Geophysical Research (1896-1977)*, *77*(19), 3592–3597, doi:https://doi.org/10.1029/JA077i019p03592.

Spenner, K., W. C. Knudsen, R. C. Whitten, P. F. Michelson, K. L. Miller, and V. Novak (1981), On the maintenance of the venus nightside ionosphere: Electron precipitation and plasma transport, *Journal of Geophysical Research: Space Physics*, *86*(A11), 9170–9178,

doi:https://doi.org/10.1029/JA086iA11p09170.

Stolzenbach, A., F. Lefèvre, S. Lebonnois, and A. Määttänen (2023), Three-dimensional modeling of venus photochemistry and clouds, *Icarus*, *395*, 115,447, doi:https://doi.org/10.1016/j.icarus.2023.115447.

Taylor, F.W., Svedhem, H., and Head, J. W. (2018), Venus: The atmosphere, climate, surface, interior and near-space environment of an earth-like planet, *Space Science Reviews*, *214*, doi:10.1007/s11214-018-0467-8.

Taylor Jr., H. A., H. C. Brinton, S. J. Bauer, R. E. Hartle, P. A. Cloutier, and R. E. Daniell Jr. (1980), Global observations of the composition and dynamics of the ionosphere of venus: Implications for the solar wind interaction, *Journal of Geophysical Research: Space Physics*, *85*(A13), 7765–7777, doi:https://doi.org/10.1029/JA085iA13p07765.

Theis, R. F., and L. H. Brace (1993), Solar cycle variations of electron density and temperature in the venusian nightside ionosphere, *Geophysical Research Letters*, *20*(23), 2719–2722, doi:https://doi.org/10.1029/93GL02485.

Theis, R. F., L. H. Brace, R. C. Elphic, and H. G. Mayr (1984), New empirical models of the electron temperature and density in the venus ionosphere with application to transterminator flow, *Journal of Geophysical Research: Space Physics*, *89*(A3), 1477–1488, doi:https://doi.org/10.1029/JA089iA03p01477.

Thiemann, E. M. B., P. C. Chamberlin, F. G. Eparvier, B. Templeman, T. N. Woods, S. W. Bougher, and B. M. Jakosky (2017), The maven euvm model of solar spectral irradiance variability at mars: Algorithms and results, *Journal of Geophysical Research: Space Physics*, *122*(3), 2748–2767, doi:https://doi.org/10.1002/2016JA023512.

Woods, T. N., F. G. Eparvier, S. M. Bailey, P. C. Chamberlin, J. Lean, G. J. Rottman, S. C. Solomon, W. K. Tobiska, and D. L. Woodraska (2005), Solar euv experiment (see): Mission overview and first results, *Journal of Geophysical Research: Space Physics*, *110*(A1), doi:https://doi.org/10.1029/2004JA010765.

Zhu, Z., J. M. Stone, and R. R. Rafikov (2013), Low-mass planets in protoplanetary disks with net vertical magnetic fields: The planetary wake and gap opening, *The Astrophysical Journal*, *768*(2), 143, doi:10.1088/0004-637X/768/2/143.

Appendix A: Chemistry Reaction Rates

The reaction rate for some chemical equations from Table 3:

(R11) $N(^4S) + O \rightarrow NO$

$$1.9 \times 10^{-23} \sqrt{\frac{300}{T_n}} (1 - \frac{0.57}{\sqrt{T_n}})$$

(R21) $N_2^+ + O \rightarrow NO^+ + N(^2D)$

$$1.33 \times 10^{-16} (300/T_i)^{0.44}$$

(R27) $N_2^+ + e \rightarrow 2N(^2D)$

$$1.01 \times 10^{-13} (300/T_e)^{0.39}$$

Figure 1.

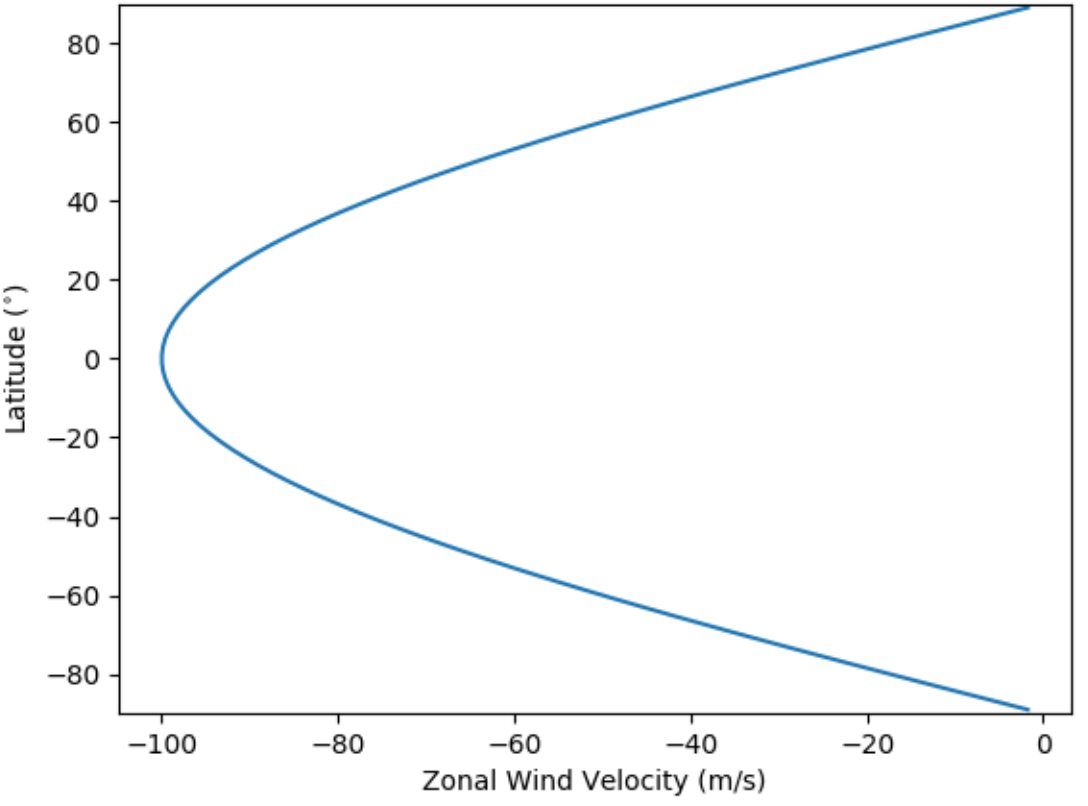
80
60
40
20
0
−20
−40
−60
−80
Latitude (°)
−100
−80
−60
−40
−20
0
Zonal Wind Velocity (m/s)

Figure 2.

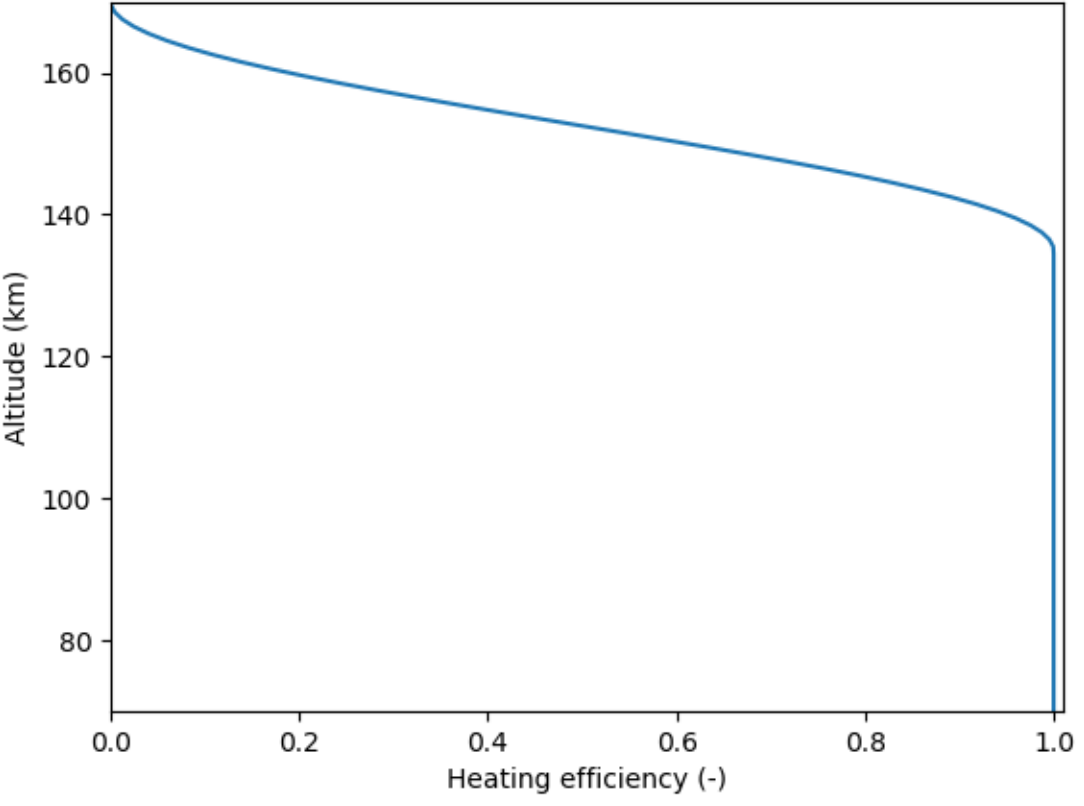
160
140
120
100
80
Altitude (km)
0.0
0.2
0.4
0.6
0.8
1.0
Heating efficiency (-)

Figure 3.

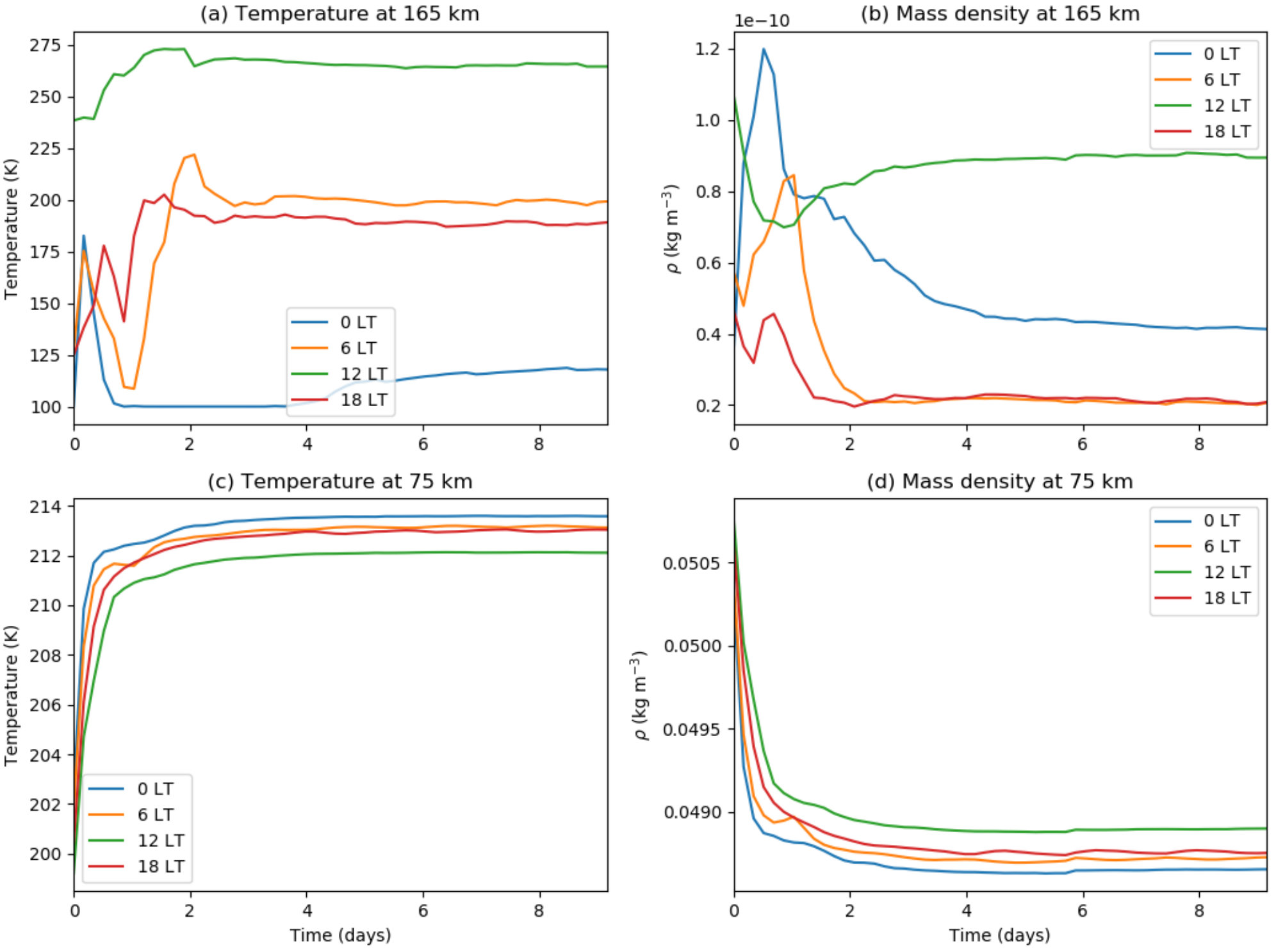
(a) Temperature at 165 km
Temperature (K)
275
250
225
200
175
150
125
100
0
2
4
6
8
0 LT
6 LT
12 LT
18 LT
(b) Mass density at 165 km
1e−10
1.2
1.0
0.8
0.6
0.4
0.2
ρ (kg m−3)
(c) Temperature at 75 km
214
212
210
208
206
204
202
200
Time (days)
(d) Mass density at 75 km
0.0505
0.0500
0.0495
0.0490

Figure 4.

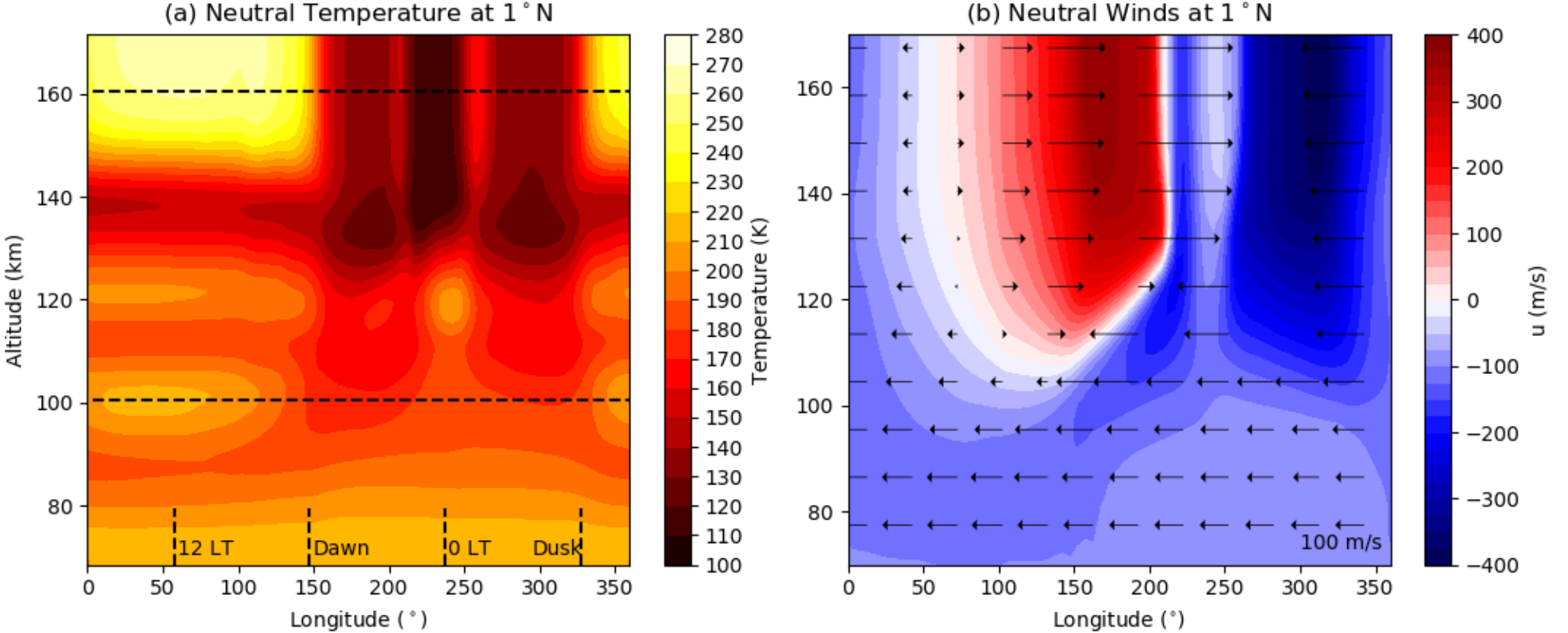
(a) Neutral Temperature at 1 ˚ N
Altitude (km)
160
140
120
100
80
12 LT
Dawn
0 LT
Dusk
0
50
100
150
200
250
300
350
Longitude (˚)
280
270
260
250
240
230
220
210
200
190
180
170
160
150
140
130
120
110
100
Temperature (K)
(b) Neutral Winds at 1 ˚ N
160
140
120
100
80
100 m/s
0
50
100
150
200
250
300
350
Longitude (˚)
400
300
200
100
0
−100
−200
−300
−400
u (m/s)

Figure 5.

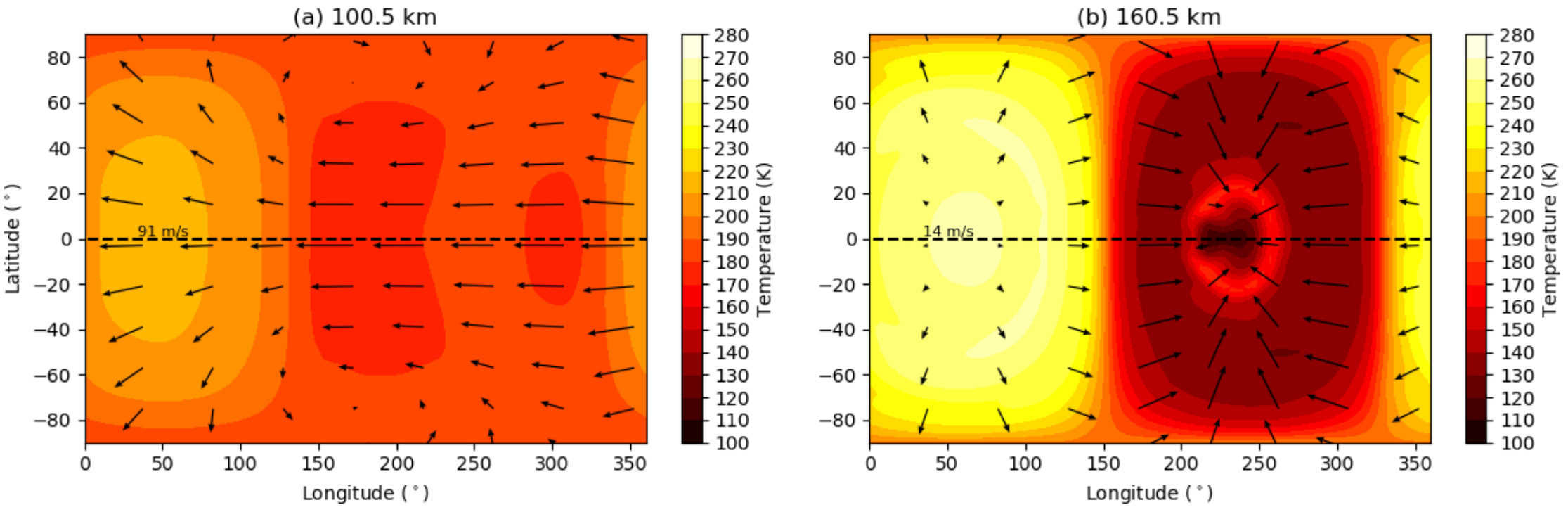
(a) 100.5 km
(b) 160.5 km
Latitude (°)
Longitude (°)
Temperature (K)
91 m/s
14 m/s
80
60
40
20
0
−20
−40
−60
−80
0
50
100
150
200
250
300
350
280
270
260
250
240
230
220
210
200
190
180
170
160
150
140
130
120
110
100

Figure 6.

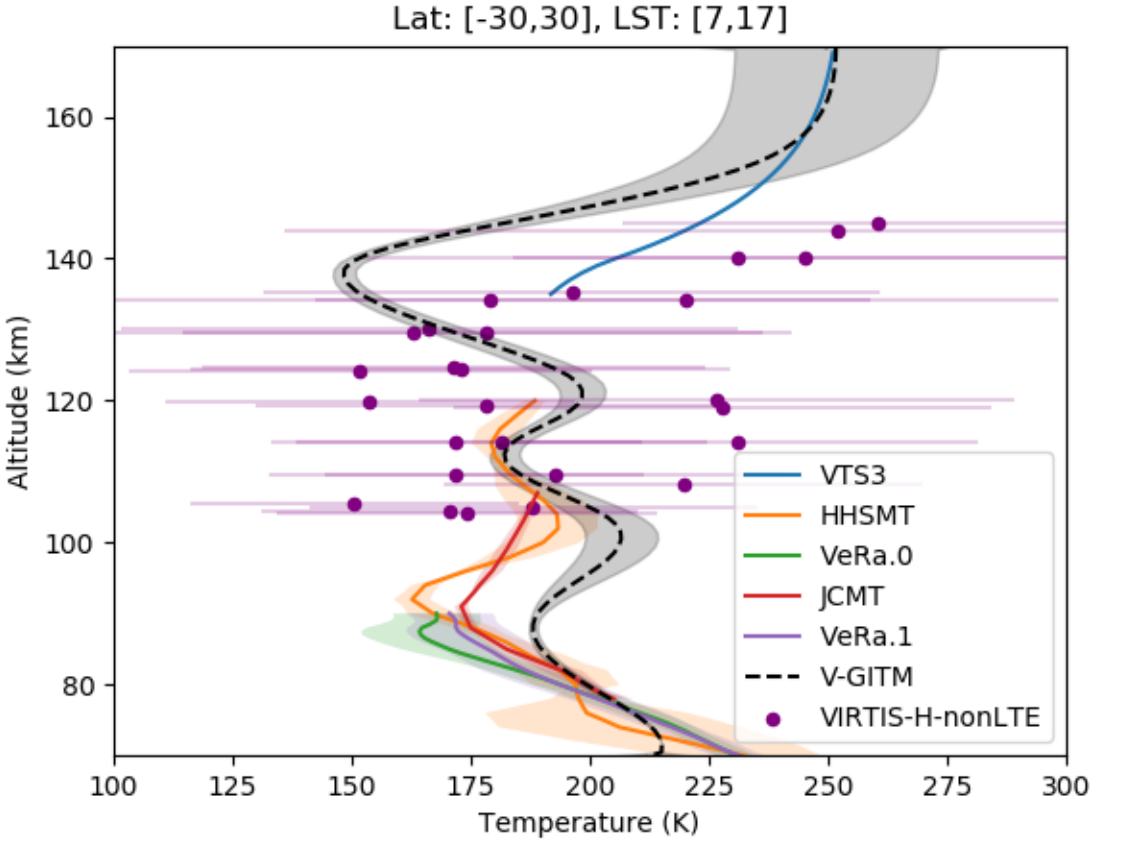
Lat: [-30,30], LST: [7,17]
Altitude (km)
160
140
120
100
80
100
125
150
175
200
225
250
275
300
Temperature (K)
VTS3
HHSMT
VeRa.0
JCMT
VeRa.1
V-GITM
VIRTIS-H-nonLTE

Figure 7.

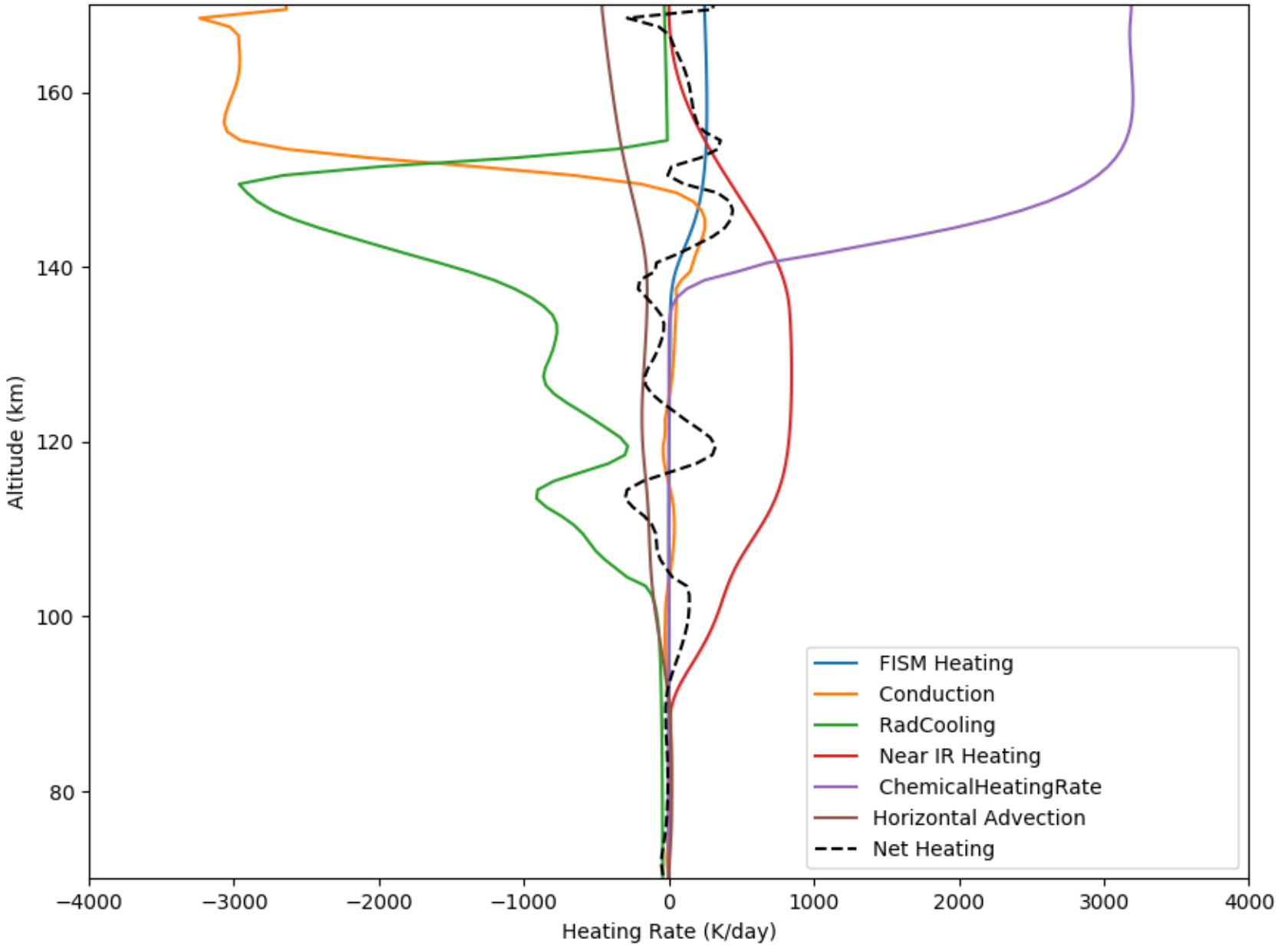
Altitude (km)
160
140
120
100
80
−4000
−3000
−2000
−1000
0
1000
2000
3000
4000
Heating Rate (K/day)
FISM Heating
Conduction
RadCooling
Near IR Heating
ChemicalHeatingRate
Horizontal Advection
Net Heating

Figure 8.

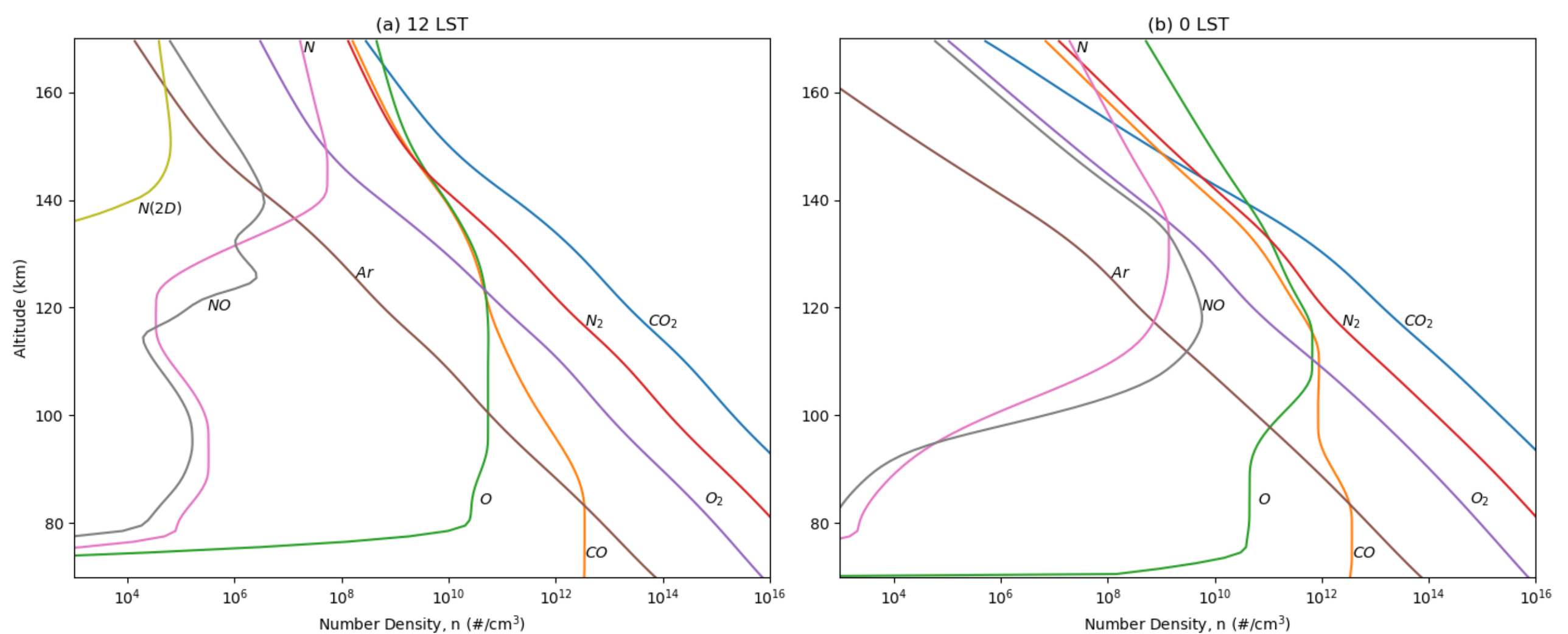
(a) 12 LST
(b) 0 LST
Altitude (km)
160
140
120
100
80
N
N(2D)
Ar
NO
N2
CO2
O2
O
CO
10^4
10^6
10^8
10^10
10^12
10^14
10^16
Number Density, n (#/cm^3)

Figure 9.

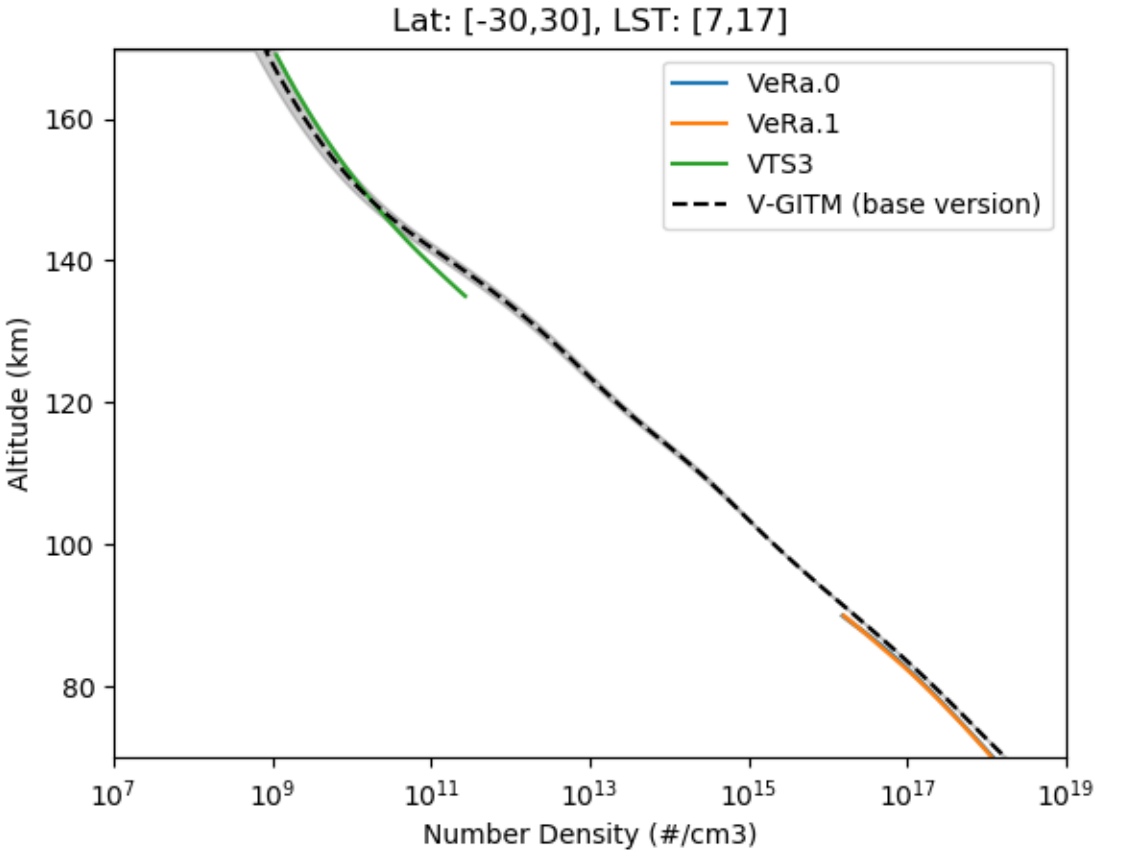
Lat: [-30,30], LST: [7,17]
VeRa.0
VeRa.1
VTS3
V-GITM (base version)
Altitude (km)
160
140
120
100
80
10^{7}
10^{9}
10^{11}
10^{13}
10^{15}
10^{17}
10^{19}
Number Density (#/cm3)

Figure 10.

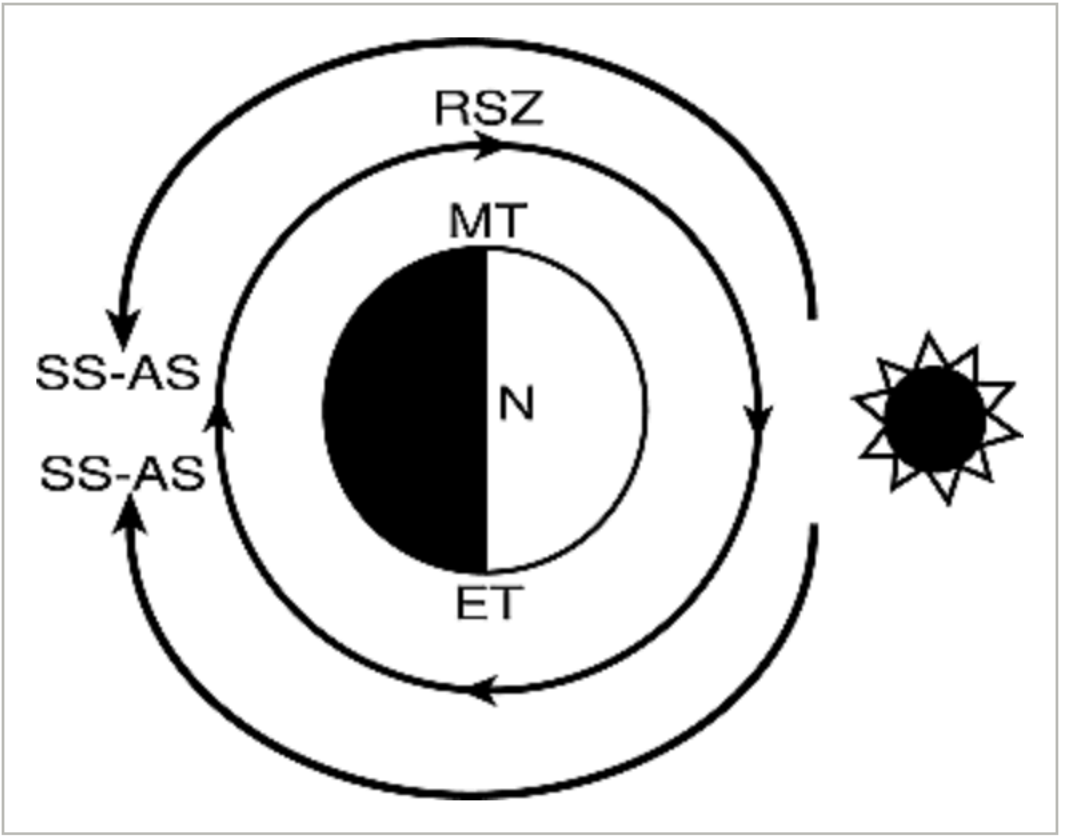
RSZ
MT
SS-AS
N
SS-AS
ET

Figure 11.

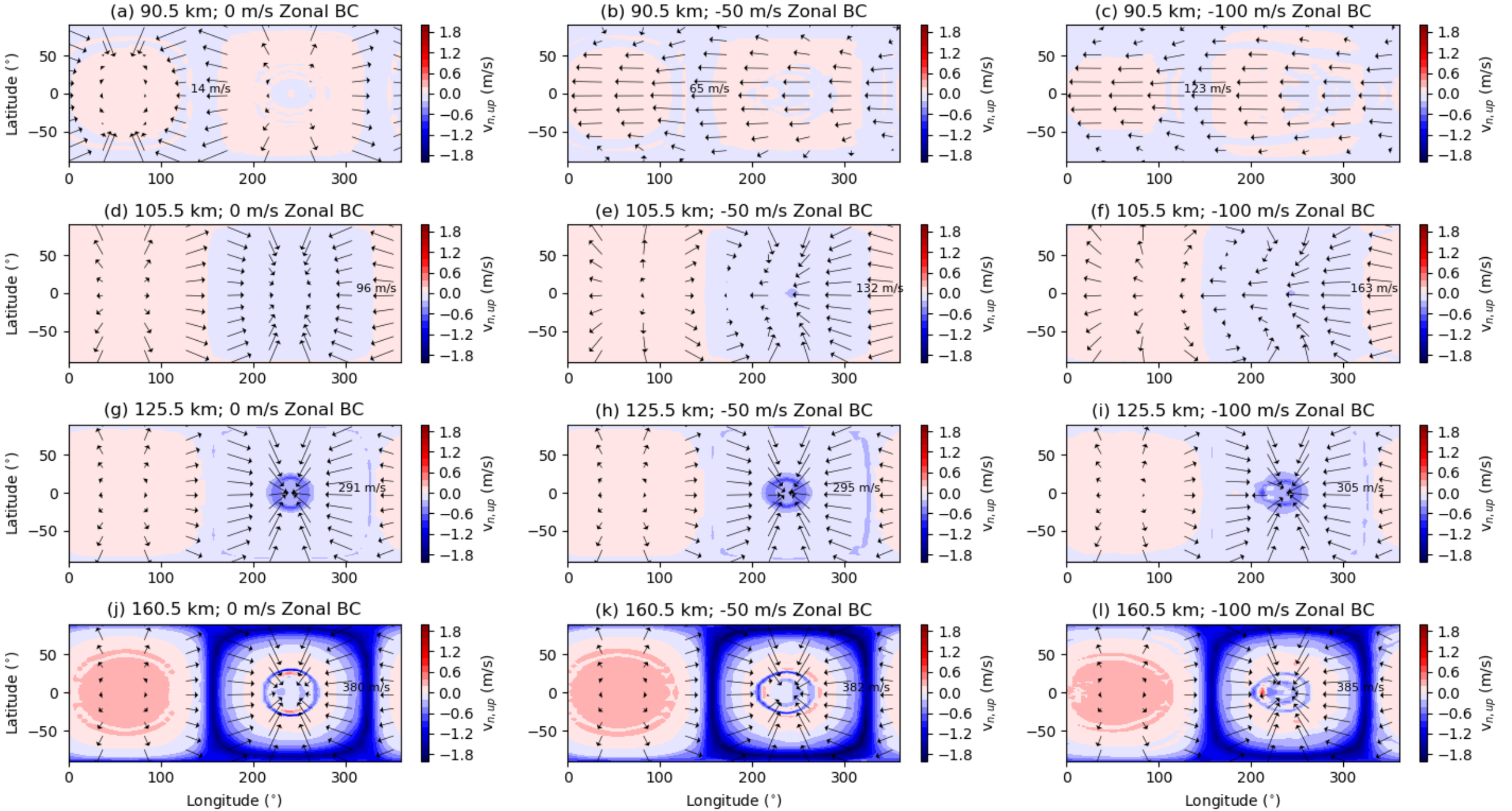
(a) 90.5 km; 0 m/s Zonal BC
14 m/s
(b) 90.5 km; -50 m/s Zonal BC
65 m/s
(c) 90.5 km; -100 m/s Zonal BC
123 m/s
(d) 105.5 km; 0 m/s Zonal BC
96 m/s
(e) 105.5 km; -50 m/s Zonal BC
132 m/s
(f) 105.5 km; -100 m/s Zonal BC
163 m/s
(g) 125.5 km; 0 m/s Zonal BC
291 m/s
(h) 125.5 km; -50 m/s Zonal BC
295 m/s
(i) 125.5 km; -100 m/s Zonal BC
305 m/s
(j) 160.5 km; 0 m/s Zonal BC
380 m/s
(k) 160.5 km; -50 m/s Zonal BC
382 m/s
(l) 160.5 km; -100 m/s Zonal BC
385 m/s
Latitude (°)
Longitude (°)
$v_{n,up}$ (m/s)
1.8
1.2
0.6
0.0
−0.6
−1.2
−1.8
50
0
−50
0
100
200
300

Figure 12.

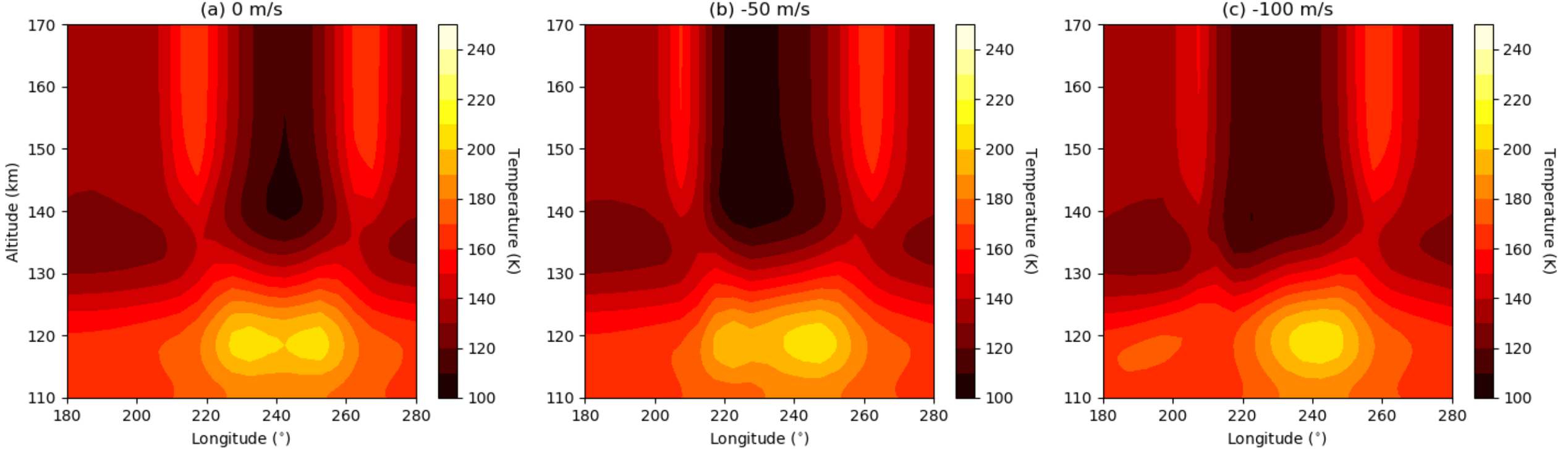
(a) 0 m/s
(b) -50 m/s
(c) -100 m/s
Altitude (km)
Longitude (°)
Temperature (K)
170
160
150
140
130
120
110
180
200
220
240
260
280
240
220
200
180
160
140
120
100

Figure 13.

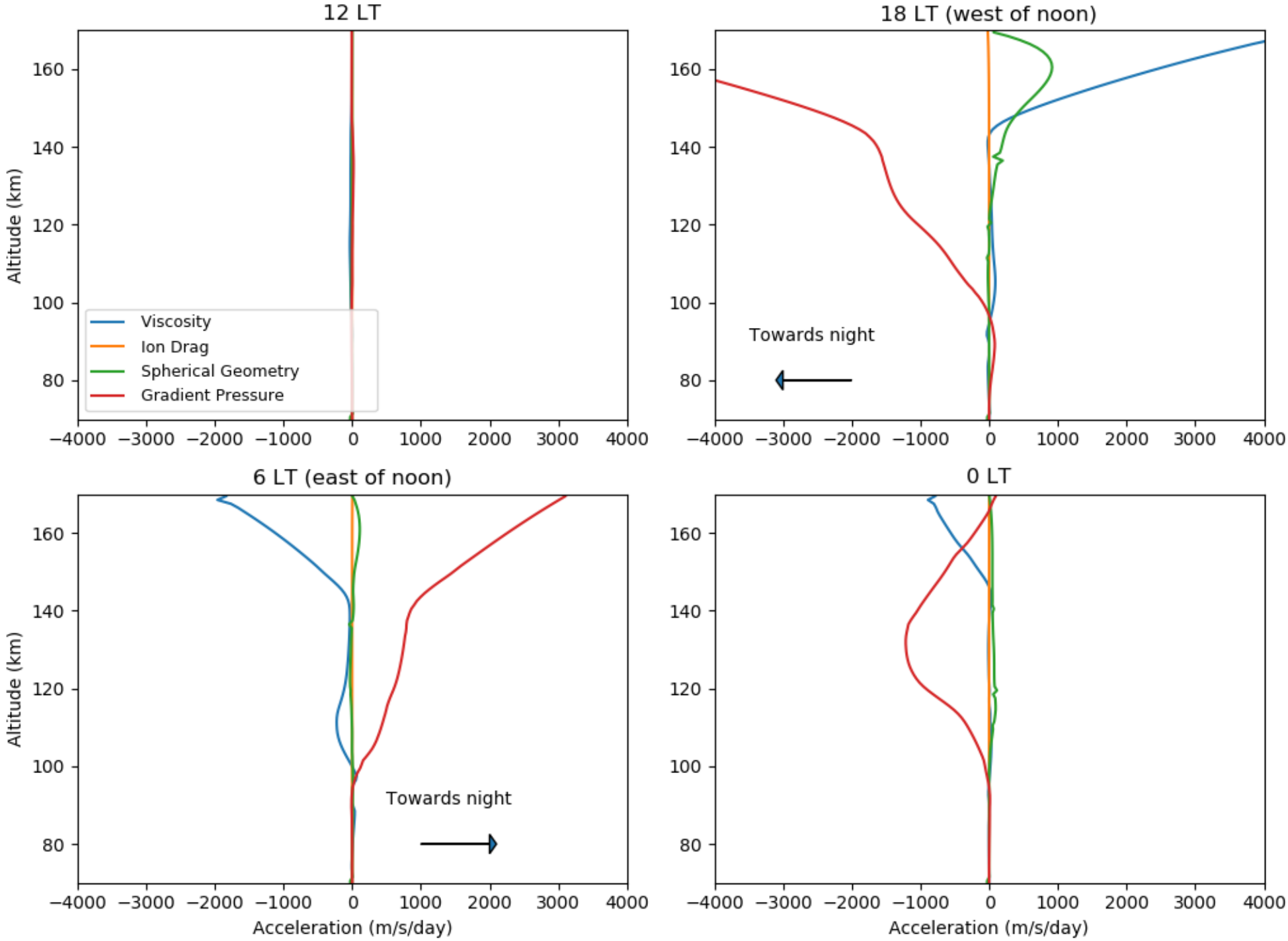
12 LT
18 LT (west of noon)
6 LT (east of noon)
0 LT
Altitude (km)
Acceleration (m/s/day)
Viscosity
Ion Drag
Spherical Geometry
Gradient Pressure
Towards night
Towards night
160
140
120
100
80
−4000
−3000
−2000
−1000
0
1000
2000
3000
4000

Figure 14.

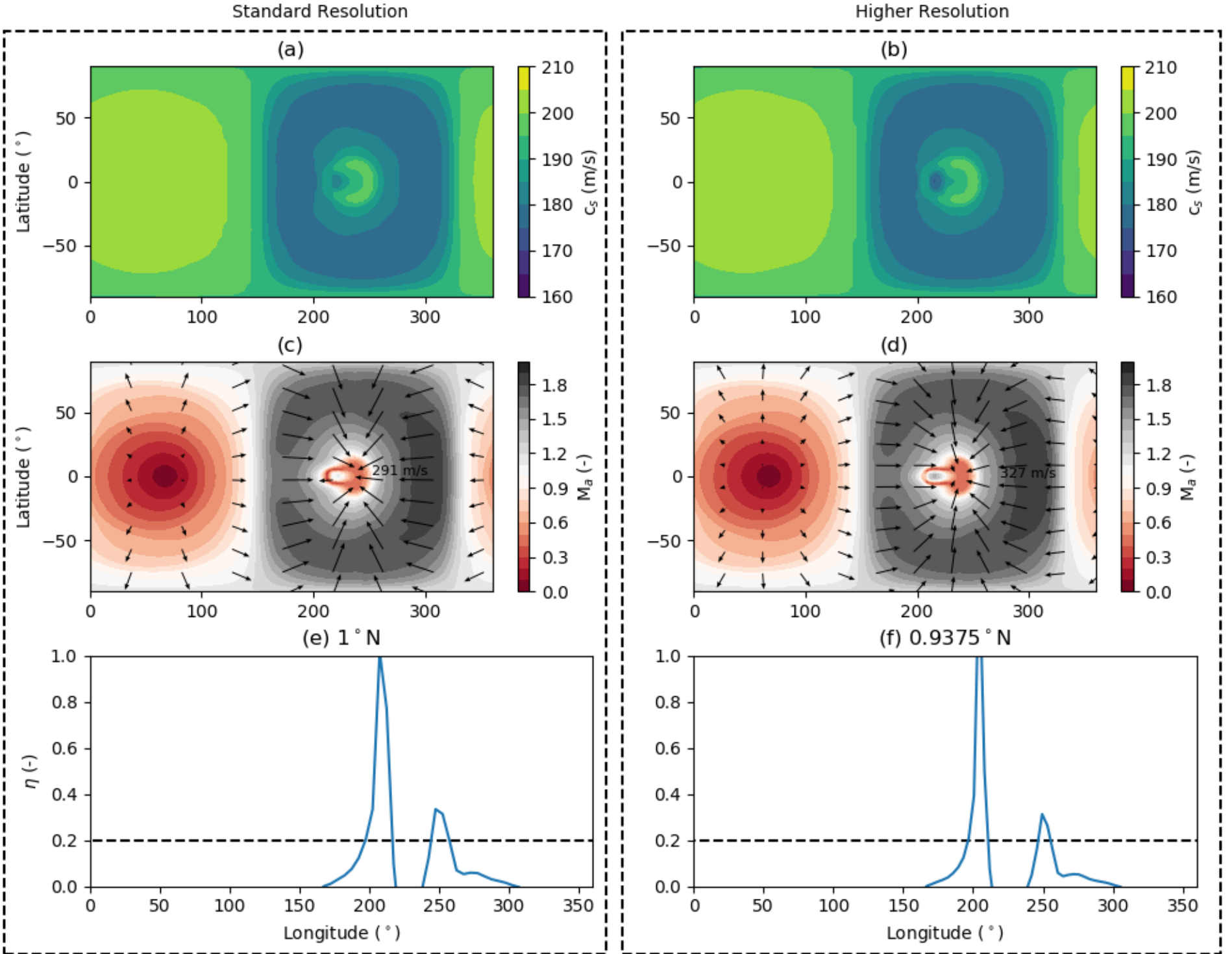
Standard Resolution
Higher Resolution
(a)
(b)
(c)
(d)
(e) 1 ° N
(f) 0.9375 ° N
Latitude (°)
Longitude (°)
c_s (m/s)
M_a (-)
η (-)
291 m/s
327 m/s

Figure 15.

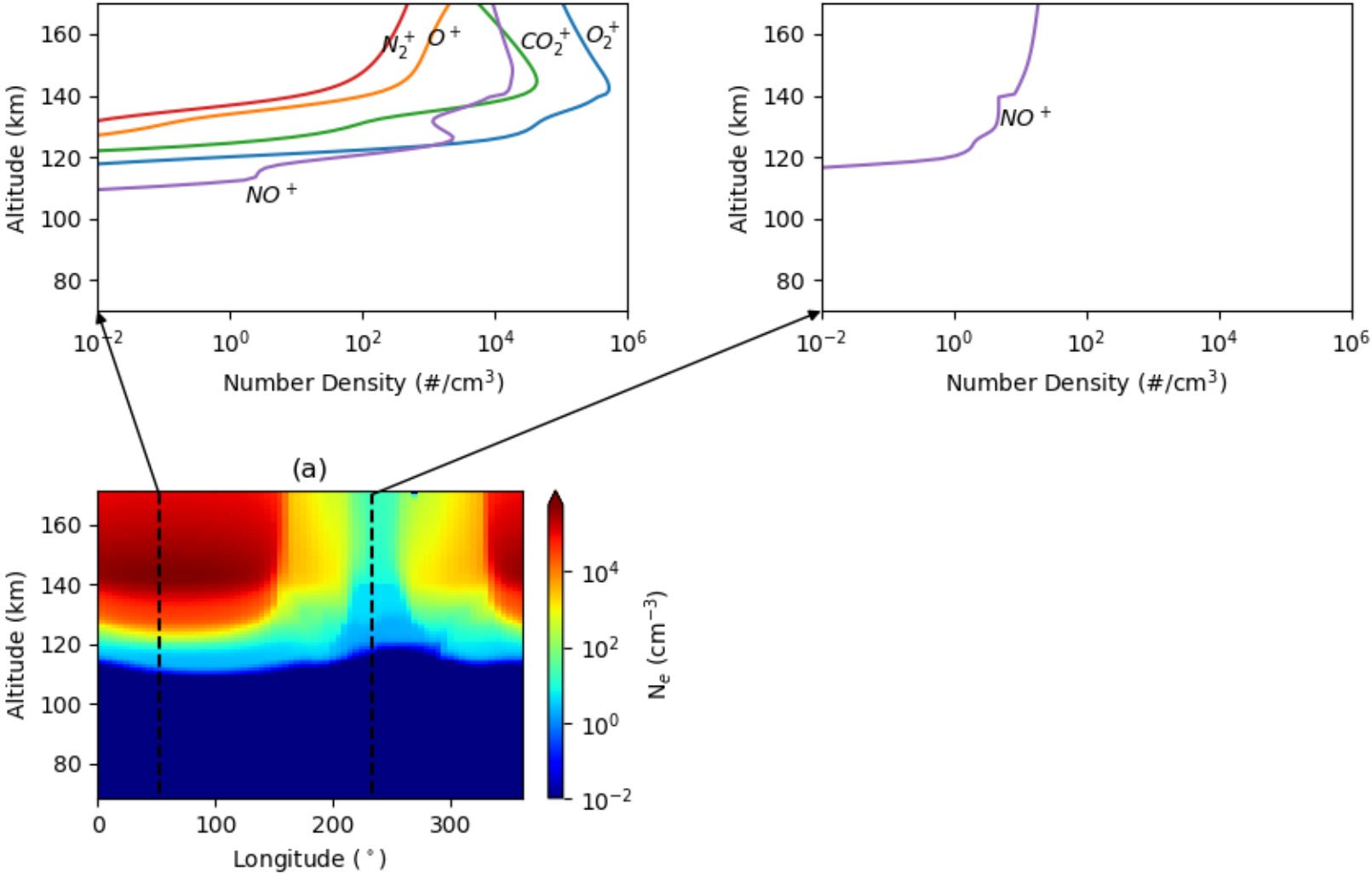
Altitude (km)
160
140
120
100
80
N_2^+
O^+
CO_2^+
O_2^+
NO^+
10^{-2}
10^0
10^2
10^4
10^6
Number Density (#/cm^3)
(a)
0
100
200
300
Longitude (°)
10^4
10^2
10^0
10^{-2}
N_e (cm^{-3})

Figure 16.

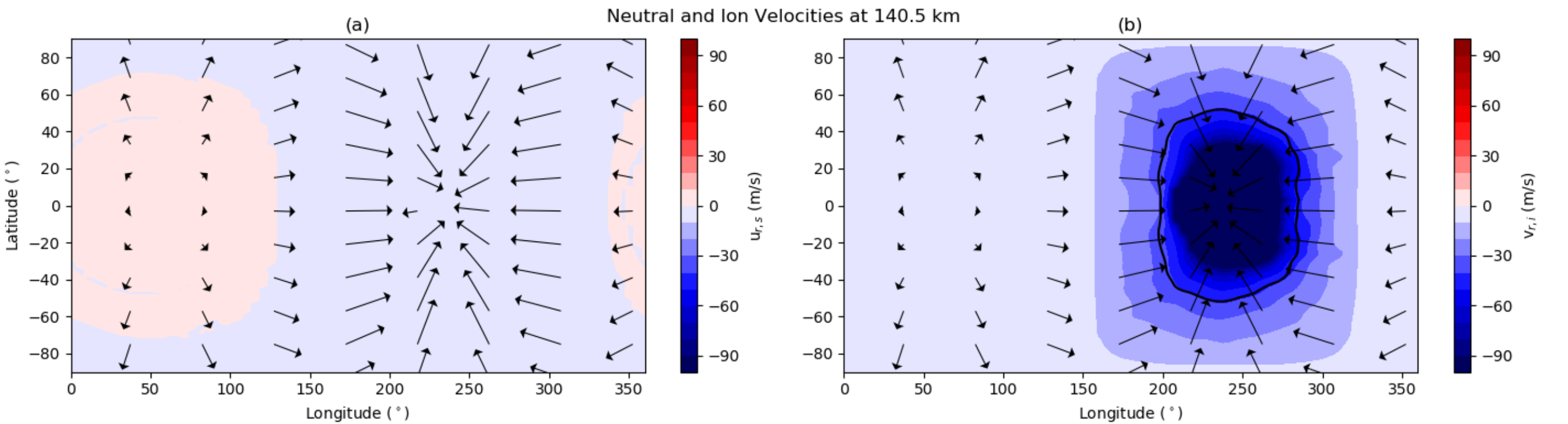
Neutral and Ion Velocities at 140.5 km
(a)
(b)
Latitude (°)
Longitude (°)
Longitude (°)
80
60
40
20
0
−20
−40
−60
−80
0
50
100
150
200
250
300
350
90
60
30
0
−30
−60
−90
$u_{r,s}$ (m/s)
$v_{r,i}$ (m/s)

Figure 17.

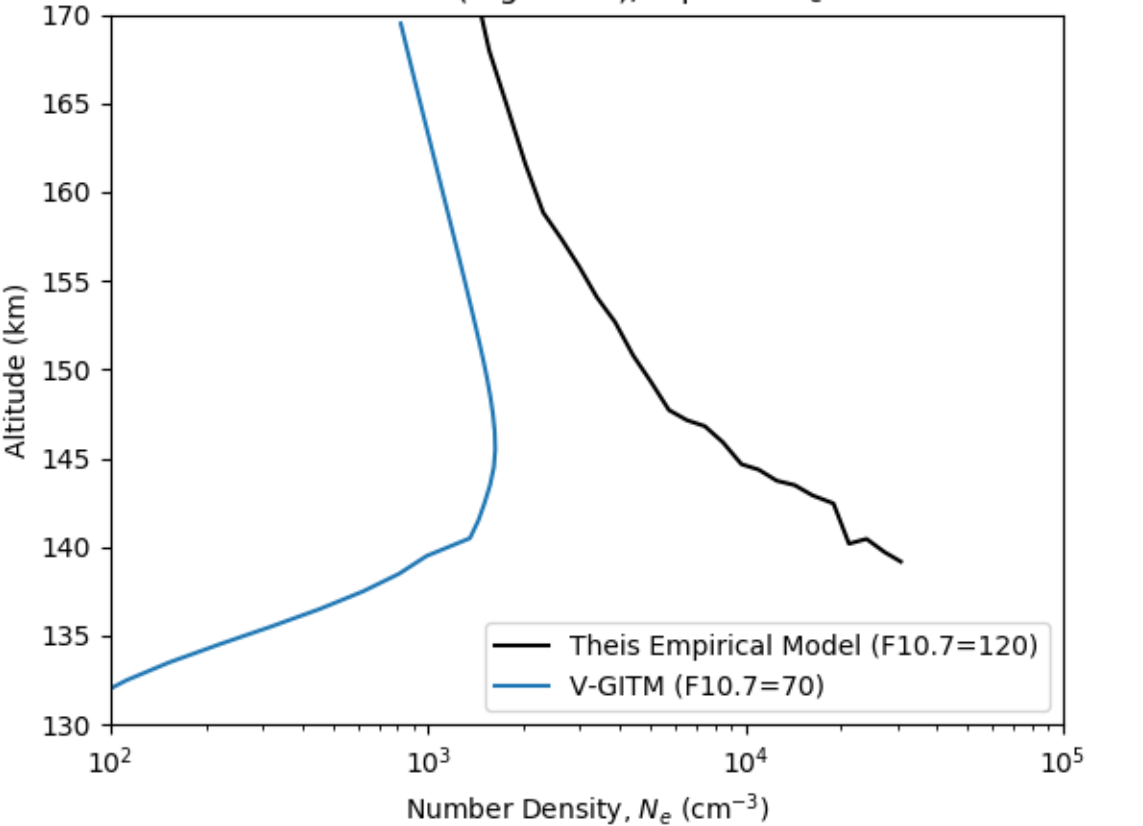
2.5 LT (nightside), Equator N_e
Altitude (km)
170
165
160
155
150
145
140
135
130
10^2
10^3
10^4
10^5
Number Density, N_e (cm^{-3})
Theis Empirical Model (F10.7=120)
V-GITM (F10.7=70)